SKI Report 2004:52

Research

Phenomenological Studies on Melt-Structure-Water Interactions (MSWI) during Postulated Severe Accidents

B.R. Sehgal
H.S. Park
A. Giri
A. Karbojian
A. Jasiulevicius
R.C. Hansson
U. Chikkanagoudar
D. Shiferaw
A. Stepanyan

January 2004

ISSN 1104–1374
ISRN SKI-R-04/52-SE

SKI

The APRI 5 (Accident Phenomena of Risk Importance) research project is accomplished by:

- Swedish Nuclear Power Inspectorate
- Ringhals AB
- OKG Aktiebolag
- Forsmarks Kraftgrupp AB
- Barsebäck Kraft AB

and supervised by the Project Board, consisting of:

OKG Aktiebolag	Mauritz Gärdinge, chairman
Swedish Nuclear Power Inspectorate	Oddbjörn Sandervåg
Swedish Nuclear Power Inspectorate	Ninos Garis
Ringhals AB	Anders Henoch
Forsmarks Kraftgrupp AB	Ingvar Berglund
Barsebäcks Kraft AB	Erik Larsen
Agrenius Ingenjörsbyrå	Lennart Agrenius (project leader)

SKI Report 2004:52

Research

Phenomenological Studies on Melt-Structure-Water Interactions (MSWI) during Postulated Severe Accidents

B.R. Sehgal
H.S. Park
A. Giri
A. Karbojian
A. Jasiulevicius
R.C. Hansson
U. Chikkanagoudar
D. Shiferaw
A. Stepanyan

Division of Nuclear Power Safety
Department of Energy Technology
Royal Institute of Technology
SE-100 44 Stockholm
Sweden

January 2004

SKI Project Number 23134

CONTENT

SUMMARY

This is the annual report for the work performed in year 2003 in the research project "Melt-Structure-Water Interactions (MSWI) During Severe Accidents in LWRs", under the auspices of the APRI Project, jointly funded by SKI, HSK, and the Swedish and Finnish power companies. The emphasis of the work was placed on phenomena and parameters, which govern the droplet fragmentation in steam explosions, in-vessel and ex-vessel melt/debris coolability, melt pool convection, and the thermal and mechanical loadings of a pressure vessel during melt-vessel interaction.

Most research projects in 2002, such as the COMECO, POMECO and MISTEE programs, were continued. An analysis of the FOREVER experiments using the RELAP code to investigate the melt coolability, bubble dynamics and bubble stability to investigate the dynamic behavior of vapor bubble during steam explosions and associated melt fragmentation, quenching boiling experiment to investigate the thermal behavior of single melt droplet were newly initiated. The SIMECO experiment to investigate the three-layer melt pool convection was restarted. The experimental facilities for these projects were fully functional during year 2003. Many of the investigations performed during the course of the MSWI project have produced papers, which have been published in the proceedings of technical meetings and Journals.

Significant technical advances were achieved during the course of these studies. These were:

- A series of experiments on single drop steam explosions was performed to investigate the fine fragmentation process of a metallic melt drop in various thermal conditions. For the first time, transient fine fragmentation process of a melt drop during explosion phase of a steam explosion was visualized continuously and quantified. Different triggering behavior with respect to the coolant subcooling was observed.

- The analyses on bubble dynamics during a single drop steam explosion and vapor bubble stability estimated the dynamic pressure generation and associated melt fragmentation. Approximately 70% of a melt drop was fragmented until the second bubble collapses during the steam explosion process.

- The quenching experiments employing a hot sphere, which dropped into coolant were performed to investigate the thermal behavior, e.g., direct contact boiling heat transfer, film boiling heat transfer etc., of the melt droplet prior to the triggering of steam explosion and consequently to provide the database to develop a theoretical model for the quenching boiling heat transfer.

- The POMECO experiments revealed the significant additional cooling capability in the debris bed when the control rod guide tubes were used to inject cooling water, showing the enhancement of the dryout heat flux and quenching rates.

- The COMECO tests showed that the presence of downcomers enhanced the quenching of the molten pool, decreasing the solidification time. Between the top and bottom addition of water, the bottom cooling dominates the cooling process. In the case of cooling with no downcomer, a strong effect of the injected gas velocity on the quenching (solidification) process was obtained. The effect of the downcomer was not as significant as that indicated in the POMECO tests.

- The SIMECO experiments were restarted to investigate the melt pool convection in multi-layer configuration which has metallic melt layers on the top and bottom and oxidic melt layer in the middle of the melt pool. The experimental results were compared to those from the previous SIMECO experiments with the uniform and two/layer melt pool configuration.

- The FOREVER-EC6 test in which water was injected on the top of the melt pool during the vessel creep was analyzed to investigate the important heat transfer parameters using the RELAP code. The analysis showed that the melt top and surface heat flux decreases with time due to the crust formation and that it is not possible to quench the melt pool with water flooding from top.

1. INTRODUCTION AND RESEARCH ACTIVITIES

This report presents descriptions of the major results obtained in the research program "Melt-Structure-Water Interaction (MSWI)" at NPS/RIT during year 2003. The primary objectives of the MSWI Project in year 2003 were to study:

- The in-vessel melt coolability process when the lower head with full of melt is flooded with water.
- The enhancement of in-vessel debris and melt coolability with heat removal through control rod guide tubes.
- The ex-vessel melt pool coolability process and the enhancement of coolability through water addition in downcomers.
- The in-vessel melt pool convection when the melt pool in the lower head forms multi-layer configuration.
- The droplet triggering and fragmentation process that occurs when a melt droplet is discharged into a water pool.
- The thermal and hydrodynamic behavior of a melt droplet during the quenching process.

Associated objectives were to (1) establish scaling relationships so that the data obtained in the experiments could be extended to prototypical accident geometries and conditions, (2) develop phenomenological or computational models for the processes under investigation and (3) validate the existing and newly-developed models against data obtained at RIT and at other laboratories.

In 2003, several experimental programs in 2002, such as the COMECO (COrium MElt COolability), POMECO (POrous MEdia COolability) and MISTEE (Micro-Interactions in STeam Explosion Experiments) programs were continued. The FOREVER (Failure Of REactor VEssel Retention) research project was completed in 2002. The SIMECO (SImulation of MElt Coolability) program was restarted and will be continued in 2004. A larger version of the POMECO (POrous MEdia COolability) facility is in the design stage in 2003 and will be built in 2004 wherein 3-D effects on debris coolability will be studied.

In this report, the experimental results from the COMECO, POMECO, SIMECO and MISTEE experiments as well as analytical results on droplet deformation, bubble dynamics during the steam explosion, and melt coolability during the FOREVER experiments, using the RELAP code, will be described.

2. SINGLE DROP STEAM EXPLOSION: MISTEE EXPERIMENTS

2.1 INTRODUCTION

Our research activities on Molten Fuel-Coolant Interactions (MFCI) continue experimentally and analytically to investigate the detailed triggering and fine fragmentation mechanisms of steam explosions. A test facility of single drop steam explosion has been constructed and a series of tests have been successfully performed.

The research on single drop steam explosions at NPS/RIT mainly aims (1) to investigate the triggerability and explosivity in a well-controlled facility of a high temperature melt droplet with an external trigger, (2) to identify the influence of melt thermo-physical properties on triggerability and explosivity of the melts, (3) to acquire quantitative data on the volume fractions of melt, coolant and vapor in the interaction zone during the fine fragmentation process in the explosions, and eventually (4) to develop scaling methodology for the explosion phase of a steam explosion.

In year 2003, a series of metallic tests with Tin as a simulant melt has been conducted. High-speed photo images synchronized with dynamic pressure signals were obtained. The effect of the coolant subcooling on the fine fragmentation were investigated. An analytical model for a stratified explosion on a single drop was developed. Image analysis was refined to quantify the transient melt fragmentation after a series of calibration tests.

2.2 SINGLE DROP STEAM EXPLOION EXPERIMENT

2.2.1 The MISTEE Facility

A facility, called **MISTEE** (**M**icro **I**nteractions in **S**team **E**xplosion **E**xperiments) shown in Figure 2.1 with a continuous high-speed X-ray radiography system is used for the single drop vapor explosion experiments. The MISTEE system consists of: a test chamber, a melt generator, an external trigger system, an operational control system, a data acquisition and the visualization system.

The test section is a rectangular stainless steel tank (180x130x250mm) with 4 view windows. At the bottom of the test section, a 1kW immersion heater is installed. A piezoelectric pressure transducer is flush-mounted at the center of the test section wall. K-type thermocouples are employed to measure temperatures of the molten droplet at the furnace and the water temperature inside the test section.

The melt generator consists of induction furnace (260V, 40A) and a graphite cylinder (40mm O.D. x 50mm) with an alumina crucible (20mm I.D. x 30mm) with a 4.1mm hole at the center of the bottom. The alumina crucible is coated with boron-nitride to provide the non-wettable surface which helps complete delivery of molten tin. Molten tin mass of 0.7g is chosen in this series of tests to guarantee the delivery of a single drop into water through the crucible bottom hole. The mass of a tin drop is accurately prepared using an electronic balance which has an accuracy of 10^{-4} g. The melt generator which includes the induction coils and the melt crucible is housed inside a container. The inner wall of the container is covered with insulator to protect the induction coil and outside housing container from excessive heat generated from the melt crucible. Argon gas purges into the container during the melting to prevent the molten tin from the

oxidation. A boron-nitride plug as a melt release plug is used to block the crucible bottom hole during the melting and is lifted by a pneumatic piston to release the melt drop.

The external trigger, located at the bottom of the test chamber, is a piston that generates a sharp pressure pulse similar to a shock wave. The trigger hammer is driven by a rapid discharge of a capacitor bank, consisting of three capacitors that impact on the piston to generate a pressure pulse.

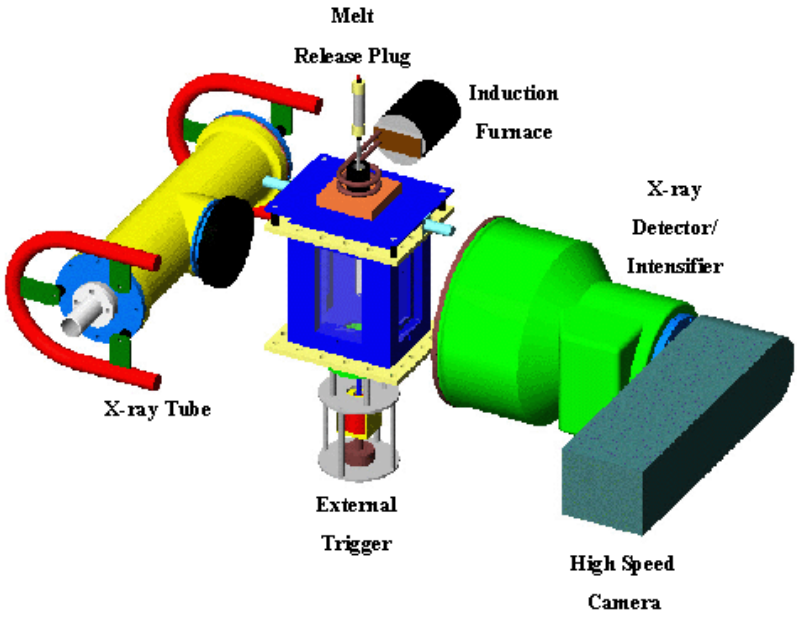

Figure 2.1: The MISTEE Facility

The visualization system of photography and radiography consists of a continuous X-ray source tube (max. 320 keV, 22mA), an X-ray converter and image intensifier and a high-speed video camera (max. 8000fps for 4 s). The resolution of the X-ray image is 56 line pairs per centimeter. The image size of the high-speed camera at 8000 fps is 80x70 pixels. Due to this small size of the image at high frame rates, the precise control of the experiments is required. In so doing, the control system employs a set of precision timers which has a time resolution of 1 ms to provide the accurate operation signals to the subsequent automatic sequences of experiments such as such as triggering of: the high-speed camera, the data acquisition system, and the external trigger system.

The MISTEE facility is located inside the 600 mm thick reinforced-concrete containment (4mx4mx4m in size) to provide the X-ray radiation shielding during the tests. The operation of the test is controlled remotely from outside of the containment. The schematic diagram of the control system is shown in Figure 2.2.

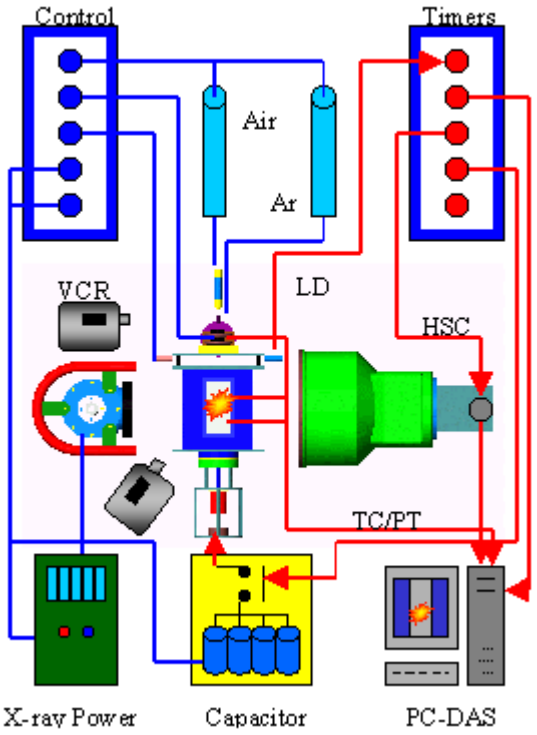

Figure 2.2: Remote Control System

2.2.2 Experimental conditions and procedure

Molten tin (Sn) and normal tap water are used as the high-temperature melt drop and the coolant, respectively. Figure 2.3 illustrates the experimental conditions in a Thermal Interaction Zone (TIZ) plot for tin-water system which have been performed. The temperatures of melt and water are set to about 1000 °C and a range of 20~90 °C, respectively. In this paper, however, the discussion will focus on the tests with highly subcooled water of about 20 °C.

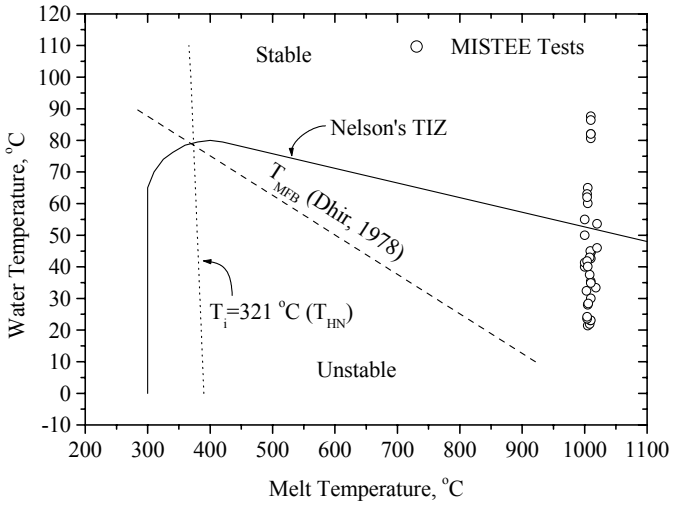

Figure 2.3: Experimental conditions in the thermal interaction zone (TIZ)

The initial thermal conditions, as shown in Figure 2.3, for the present tests are in the unstable region of the TIZ, which means that spontaneous vapor explosion may occurs at any time. Therefore all tests are externally triggered before the possible spontaneous explosion to ensure to provide the consistent triggering conditions for the single drop as well as the specific location of vapor explosions for high-speed visualization.

The experiment starts with heat up of the tin in the induction furnace. The molten drop is released into the test section filled with water by the remote operation of lifting the melt release plug. When the released tin drop cuts a horizontal line laser beam located below the furnace and 100 mm above the water surface, a photo sensor detects the laser beam disturbance and provides the reference trigger signal to the remote control system to activate subsequent operating sequences of experiments. The vapor explosion is initiated by a shock wave (up to 1.5 MPa) generated from the external trigger system attached beneath the test section. Recorded images are downloaded into a PC where the post image processing takes place.

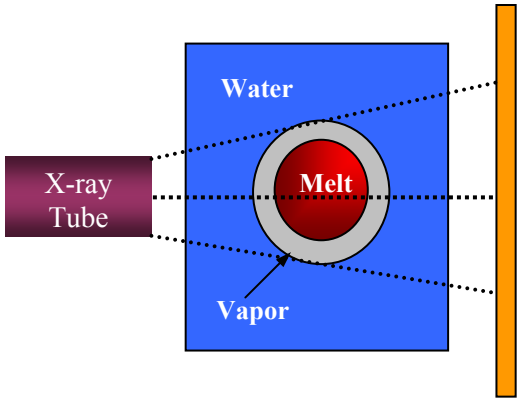

Figure 2.4: The schematic diagram of the X-ray Radiography

2.2.3 Image Processing

The intensity of the detected X-rays, I, after the transmission of the incident X-ray beams, I_o, in a medium, obeys the attenuation law as follows

$$I^{NS} = I_0 \exp\left\{-\sum_i \mu_i \delta_i\right\} \tag{2.1}$$

where, I^{NS}, δ_i and μ_i are the detected X-ray intensity without scattering in the surrounding media, the thickness and the mass attenuation coefficient of i-th materials. Total X-ray intensity detected at the converter, however, consists of the X-ray intensity without scattering, I^{NS}, and the X-ray intensity with scattering I^S,

$$I = I^{NS} + I^S \tag{2.2}$$

This transmitted X-ray beams are proportionally converted into photon beams at the converter, which are recorded into contrast images by the high-speed CCD camera in our radiography system. The image contrast proportional to the transmitted X-ray beam is transformed into digitized gray level. Therefore the digitized gray level, G, can be generally expressed as,

$$G = \alpha I + G_{DC} = \alpha\left(I^{NS} + I^{S}\right) + G_{DC}$$
$$= \alpha I_0 \exp\left\{-\sum_i \mu_i \delta_i\right\} + G^0 \tag{2.3}$$

where α, G_{DC}, and G^0 are the proportional constant, dark current of the image system and the image offset which represents the background noises of the image gray level due to the scattered X-ray beams and the CCD dark current, i.e., $\alpha I^S + G_{DC}$.

The basic arrangement of our XR system (X-ray tube and converter) with a test section that has multiphase mixture of water, vapor and melt during the vapor explosion process is shown in Figure 2.4. In this configuration, the X-ray intensities with and without melt droplet surrounded by vapor film, G_M and G_{NM}, respectively can be obtained as follows,

$$G_M = \alpha_M I_0 e^{\{-\mu_A\delta_A - \mu_{TS}\delta_{TS} - \mu_L\delta_{LM} - \mu_V\delta_V - \mu_M\delta_M\}} + G_M^0 \tag{2.4}$$

$$G_{NM} = \alpha_{NM} I_0 e^{\{-\mu_A\delta_A - \mu_{TS}\delta_{TS} - \mu_L\delta_L\}} + G_{NM}^0, \tag{2.5}$$

where the subscripts A, TS, L, LM, and V are denoted as the air, the test section, the liquid pool, the liquid pool with a melt droplet and the vapor. Since the projected area of the melt droplet in the test-section filled with liquid is significantly smaller than that of the test-section, $\alpha_M \sim \alpha_{NM} = \alpha$, $G^0_M \sim G^0_{NM} = G^0$ and $\delta_{LM} \sim \delta_L$ will be valid. In addition, since the attenuation of X-ray beam in the vapor film around the melt droplet is negligible, the equations (4) and (5) becomes

$$G_M \cong \alpha I_0 e^{\{-\mu_A\delta_A - \mu_{TS}\delta_{TS} - \mu_L\delta_L - \mu_M\delta_M\}} + G^0, \tag{2.6}$$

$$G_{NM} \cong \alpha I_0 e^{\{-\mu_A\delta_A - \mu_{TS}\delta_{TS} - \mu_L\delta_L\}} + G^0. \tag{2.7}$$

Combining the equations (6) and (7), the normalized gray level of the image can be expressed in terms of the thickness of the melt droplet as

$$\Delta G \equiv \frac{G_M - G^0}{G_{NM} - G^0} \cong e^{\{-\mu_M\delta_M\}} = \beta e^{\{-\mu_M\delta_M\}}. \tag{2.8}$$

Therefore, the thickness of the melt droplet during the vapor explosion process can be quantified after the determination of β in a series of calibration tests by,

$$\delta_M = -\frac{1}{\mu_M}\ln\frac{\Delta G}{\beta}. \tag{2.9}$$

Investigation of morphological evolution of the molten droplet during the vapor explosion can also be quantified from the enhanced X-ray images as shown in Figure 2.5. This image enhancement was carried out by a basic process, i.e., RHS in Eq. (8) which includes the elimination of background noises and image offset.

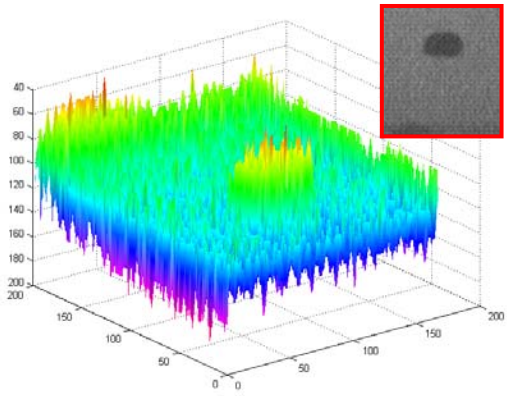

(a)

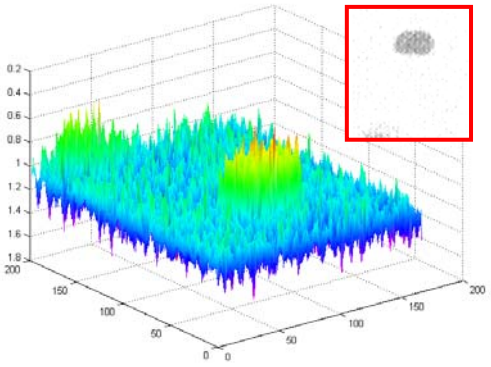

(b)

Figure 2.5: Image enhancement: (a) original image and (b) enhanced image

2.2.4 Melt Thickness Calibration

A series of calibration tests was conducted with tin foils with the various thickness of 0.025, 0.05, 0.25, 0.5, 1.0 and 2.0 mm. The calibration tests were performed by inserting these tin foils (7mm x 7mm) into the center of the water filled test section and recording the X-ray images which correspond to the specific experimental conditions since the gray levels of X-ray image vary with various experimental control parameters, such as the X-ray energy, the X-ray intensification factor, the CCD camera setting, the position of the test section, etc.

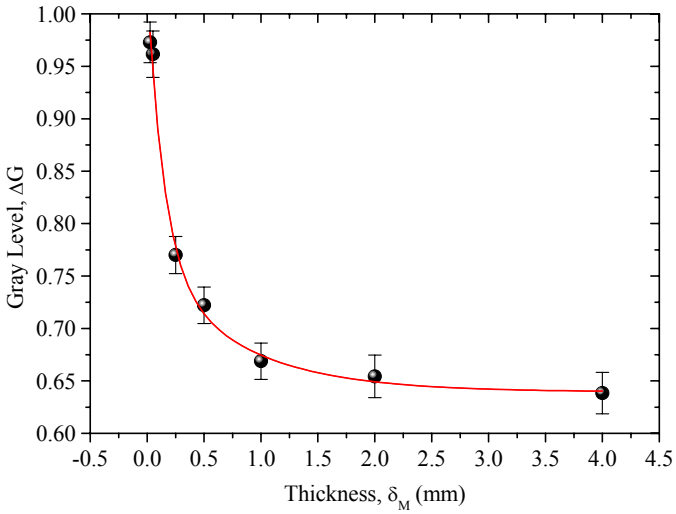

Figure 2.6: Calibration curve for the melt thickness

The gray level ratio, $(G_M - G^0)/(G_{NM} - G^0)$ is obtained by taking dark current image for G^0 and images with and without the object of interest for G_M and G_{NM}, respectively. It is noted that G^0 taken during the calibration process contains only the CCD dark current. In the present tests, scattered X-ray intensities with and without melt droplet in the test section, i.e., I^s_M and I^s_{NM}, will not be significantly different each other since the size of the melt droplet is considerably smaller than that of the test section. Therefore, during the calibration process to obtain the gray level ratio, the effect of this scattering noise due to the presence of the melt droplet can be negligible. However, the effect of the scattering noise should be considered when the different X-ray intensity energies were used.

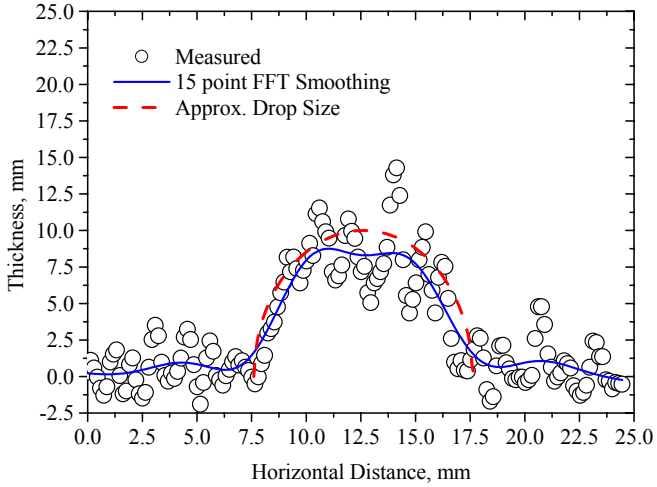

Figure 2.7: Thickness calibration of X-ray image

Figure 2.6 is the calibration curve which is utilized to convert the gray images taken from X-ray radiography to the quantitative mass or thickness distribution of the melt particles. The calibrated curve has a maximum of 3.3% deviation from the mean value. It is noted that the mass distribution represents the twe dimensional line-of-sight average values along the X-ray beam path. Figure 2.7 shows a comparison of the thickness of a melt drop before vapor explosion which is assumed to be a spherical shape (dotted line)

and actual calibrated thickness of the same drop (dot). The calibrated thickness of the droplet closely reproduced the horizontal drop size of approximately 10 mm and the thickness of the drop. In fact, there are still noises in the image which produce the fluctuation of the thickness of the drop. The solid line was obtained by performing a FFT smoothing technique with adjacent 15 points. The additional noise reduction techniques for X-ray image are still needed to improve the accuracy of this quantitative measurement.

2.3 RESULTS AND DISCUSSIONS

2.3.1 Characteristics of Single Molten Drop

The molten tin drop freely falls from the crucible in the induction furnace to the water surface. The photographic images showed that the drop was a near-spherical shape during the falling in the air and impacted on the water surface. Figure 2.7 shows that the molten tin drop travels in the air with a velocity of about 1.45 m/s and is quickly decelerated in the water down to 0.4 m/s until the explosion is triggered.

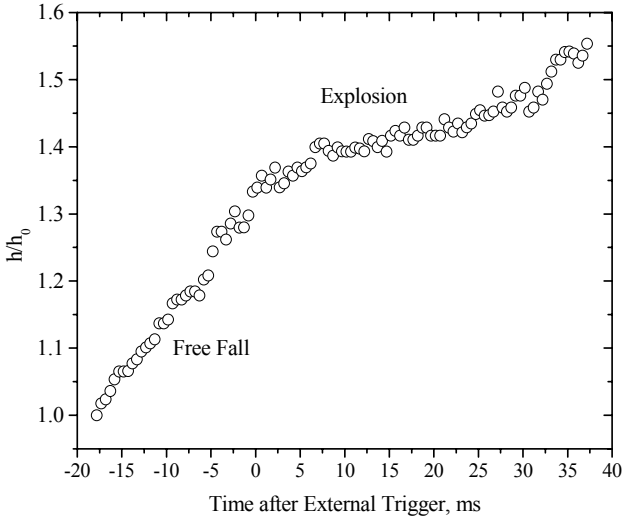

Figure 2.8: Molten tin drop trajectory

The dynamic behaviors of the molten drop in fluidic media can be described by number of dimensionless numbers, i.e., Reynolds number ($Re=\rho_f D_d u/\mu_f$), Eotvos number ($Eo=g\Delta\rho D_d^2/\sigma$), Morton number ($Mo=g\mu_f^4\Delta\rho/\rho_f^2\sigma^3$), Weber number ($We=\rho_f D_d u^2/\sigma$) and Ohnesorge number ($On=\mu_d/(\rho_d D_d \sigma)^{0.5}$) where ρ_f and ρ_d are the ambient fluid and drop densities, $\Delta\rho$ is the density difference between ρ_f and ρ_d, μ_f and μ_d are the ambient fluid and drop viscosities, σ is the surface tension, D_d is the drop diameter, g is the gravitational acceleration and u is the relative velocity between the drop and ambient fluid. In the present tests, Re, Eo, Mo, We and On numbers are in a range of $2.5\sim5\times10^3$, 3~10, $10^{-14}\sim10^{-13}$, 1~3 and $1\sim2\times10^{-4}$, respectively. These values of dimensionless numbers indicate that the molten tin drop in water is in the wobbling regime. High-speed photographic images also show that the drop falls in the water with wobbling motion from spherical to ellipsoidal spherical-cap shapes. Most of tests show that the maximum ratio of horizontal diameter to the initial diameter of the drop is about 2. Weber number and Ohnesorge number for our molten tin drop in water also indicate no drop breakup

(We_d < We_{cr}=12) and the negligible viscosity effect on the drop deformation (On<0.1) during the falling. During vapor explosions, the drop falling speed decreases from 0.4 m/s to less than 0.1 m/s. A group of fragmented particles after the vapor explosions gradually falls down with a speed of approximately 0.3 m/s.

Figure 2.9 shows a typical pressure signal obtained from the tests. Time zero was denoted as the time when the external trigger signal arrived at the center of the test section where the vapor explosion takes place. Most tests employed an external trigger of approximately 1 MPa with a rising time of less than 50μs. Major compression pressure wave, generated by vapor explosions, reaches the pressure transducer approximately 4 to 5 ms after the trigger shock disturbed the quasi-stable vapor film around the droplet. The vibration of the test section due to the impact of the external trigger piston and reflection waves of pressure signals caused the sinusoidal fluctuation (frequency of ~ 1 kHz) of the pressure signal.

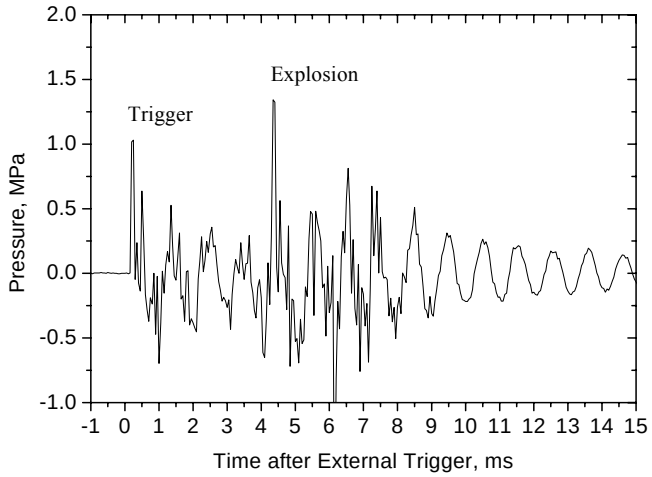

Figure 2.9: A typical pressure history for triggered vapor explosion of 0.7g tin drop at 1000 ^{o}C in water at 21 ^{o}C

2.3.2 Stratified vapor explosion in highly subcooled water

Images of vapor explosion recorded by high-speed X-ray radiography and photography at 8000 fps are shown in Figure 2.10. Time t=0 s for the images is defined as the time when the molten drop is disturbed by an external trigger shock pulse for each test. Normalized time, $\tau = t/t_c$, is used in the figure to help the comparison among images taken from different tests where t_c is the duration time for the first growth-collapse cycle of vapor bubble or melt fragmentation during the vapor explosion process.

Figure 2.10 (a) show a typical vapor explosion images taken at water temperature of 32 ^{o}C with a 0.7 g of 1000 ^{o}C molten tin drop by the high-speed photography at the frame rate of 8000 fps. At τ=0, the undisturbed molten drop is covered with vapor, showing small amount of vapor pocket on the top of the drop. The external shock pressure pulse approaches the melt drop from the bottom of the image. At τ=0.82, the melt drop is disturbed by the trigger shock wave. As indicated by an arrow in the figure, the molten drop is triggered to initiate vapor explosion at the bottom edge of the melt drop. It is

well known that this initiation of triggering of vapor explosion is resulted from a direct contact of water to the molten drop due to the collapse of surrounding vapor induced by the external trigger. This small local triggering (length scale of less than 1 mm) causes subsequent global triggering of the entire melt drop.

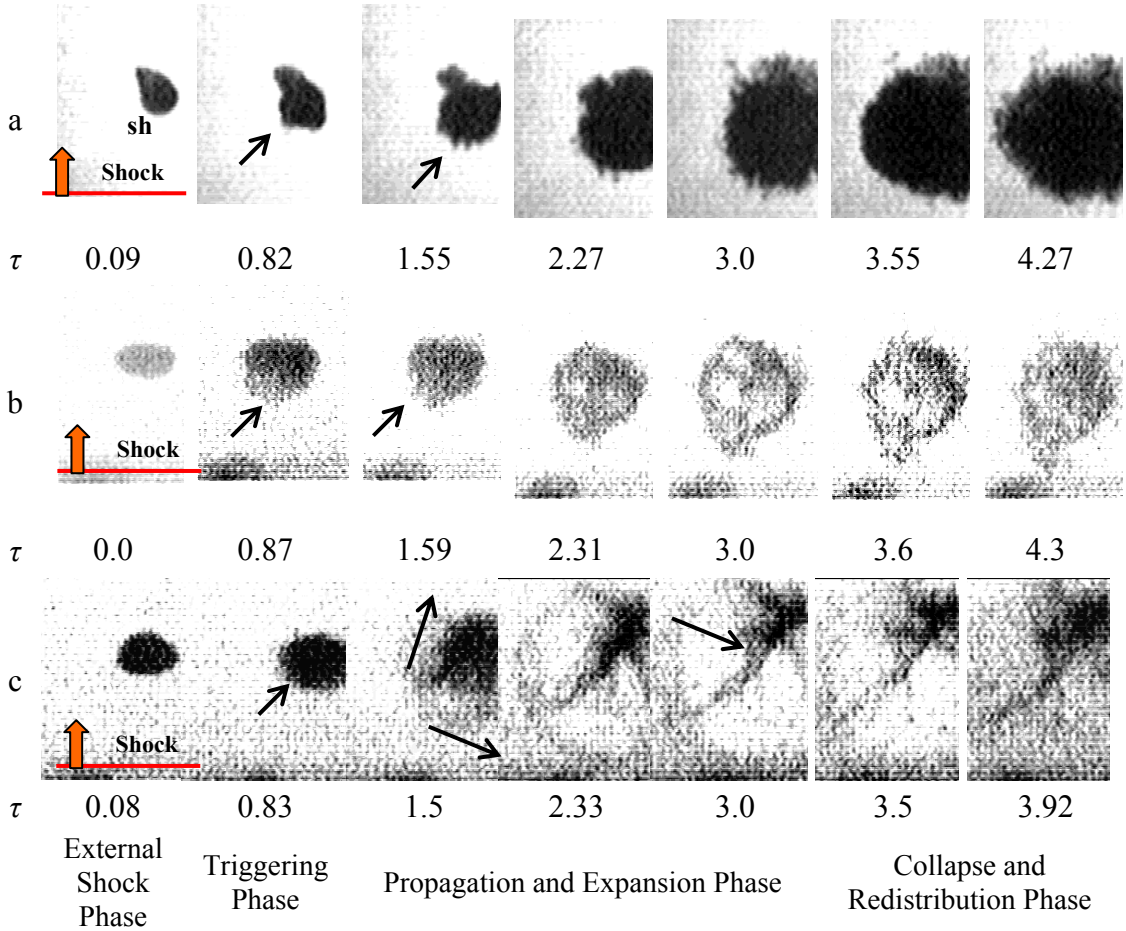

Figure 2.10. Images obtained by photographs (a) and X-ray radiographs (b, c) of the vapor explosion of 0.7 g tin drops at 1000 ^{o}C in water temperatures of 32, 22, and 21 ^{o}C, respectively.

Figure 2.11 shows a photograph for unexploded molten drops at the same experimental conditions. The drops shown in this photo are not completely exploded due to many reasons which include the oxidation on the drop surface formed during the melting process. However, this photo illustrates that the drops have a disk shape as discussed in the previous section and are triggered at one edge of these disk shape melt drops.

The time period between τ=0.82 and 1.55, a very rapid cycle of vapor expansion and collapse is observed. The image at τ=1.55 already shows the second cycle of vapor explosion and indicates wavy interface structures which is generated by a small group of finely fragmented melt particles which travel along with the boundary during the vapor expansion. At τ=2.27 and 3.0, the second and third cycles of vapor explosion are observed. Mostly the rapidest expansion of vapor is observed at the second cycle. It can be explained that this energetic vapor dynamics is caused by the vapor explosion which is promoted by the adequate mixing condition generated during the first cycle of vapor explosion. Obviously the first cycle of vapor explosion is less energetic since a part of

explosion energy must be consumed to fragment a single molten drop to numerous fine particles. Images of τ=3.0 and later show that the center of explosion is shifted from that of the first cycle. As easily recognized in this figure, these photography images provide integral vapor dynamics but limited information on the structure of melt fragmentation during the vapor explosion process.

Figure 2.10 (b) and (c) are the images taken by X-ray radiography at the near same conditions, i.e., 0.7 g of 1000 ^{o}C melt drop in room temperatures of 22 and 21 ^{o}C. These two sets of images reveal the internal structures of molten drops during the vapor explosion process. The X-ray images at τ=0 and 0.08 show the shapes of melt drops before the explosion which is invisible by photography due to the covered surrounding vapor. The shapes of the melts are near spherical and elliptical and indicate that the melt drop is in the wobbling regime as mentioned in the previous section.

Two images at τ=0.83 and 0.87 which are the near end of the first cycle of the melt dynamics due to the triggering of vapor explosion, show the deformation of melt drop due to the local initiation of explosion. In particular, the image of Figure (b) shows the dented surface (indicated by an arrow symbol in the figure) of the drop with the group of dispersed fine melt particles nearby. At τ=1.59, after the brief completion of the first cycle of melt dynamics, the ejection of melt at the same location of the previously dented drop surface. It is clearly shown in the following images that more fine particles are distributed at that area. The image at τ=3.0 shows several small scale vapor explosions inside the pre-fragmented melt drop showing several hollows.

Figure 2.10 (c) shows one of energetic vapor explosions occurred in this thermal condition and typical stratified vapor explosions on this small molten drop surface, which are normally observed in large-scale well defined stratified geometries. Comparing to the case of Figure 2.10 (b), after the first cycle of vapor explosion as shown in the images at τ=1.5 and 2.33, finely fragmented particles start dispersing from the location of the initially triggered explosion due to the stratified explosion and the explosions propagate along the drop surface. The inner unfragmented melt elongates as the explosion propagates due to the compression force produced by the stratified explosion on the melt surface.

Both tests shown in Figure 2.10 (b) and (c) show the formation of a shell of finely fragmented melt particles. The fragmented particle shell is formed at the water-vapor interface during the expansion period of vapor explosion since the larger drag force of those micro-scale particles in water than that in vapor stops the particles and accumulates in the interface. When the diameter of expanded melt particles reaches its maximum, the fragmented particles are redistributed into the interaction zone during the collapse period as shown in the images after τ=3.0 in Figure 2.10 (b) and (c). In the case of the test shown in Figure 2.10 (c), small explosions which lead to complete fragmentation of the entire melt are observed even after τ=3.92 at near the upper right corner of the image where a part of unfragmented melt still remains.

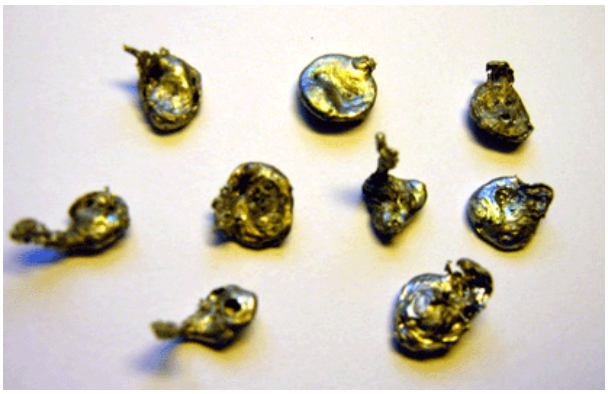

Figure 2.11: Photos of solidified molten droplets.

2.3.3 Dynamics of Vapor bubble and Melt Fragmentation

Figure 2.12 illustrates the growth history of radial bubble and fragments of 0.7 g molten tin drops at 1000 ^{o}C for different water temperatures. Our data are also compared with Nelson's data for 0.05 g of iron oxide at 1960 ^{o}C in 30 ^{o}C. In this figure, the equivalent bubble diameter, D_{eq} (area averaged diameter for the melt drops), is normalized with the equivalent diameter of the melt drop prior to the external trigger shock wave arrival.

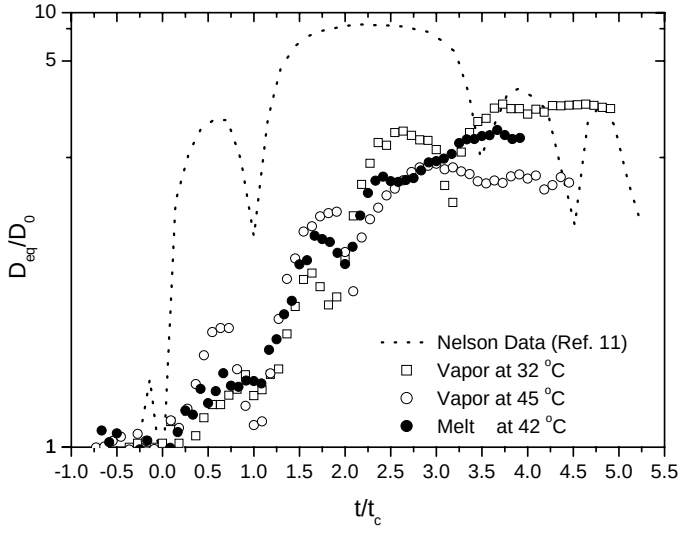

Figure 2.12: Bubble and fragment growth histories for 0.7g tin drops at 1000 ^{o}C in water at 32, 42 and 45 ^{o}C.

The maximum bubble diameters reach about 3~3.5 times the initial bubble diameters mostly after the third cycle of bubble growth-collapse. For the iron oxide melt, however, the bubble diameter becomes up to about 8 times the initial diameter. The first bubble growth and collapse take about 1.125, and 1.375 ms at water temperatures of 32 and 45 ^{o}C, respectively, which are similar to Ciccarelli's data with 0.5 g tin at 700 ^{o}C. The distribution diameter of melt fragments, at 42 ^{o}C water, completes the first cycle at 1.5 ms. The first cycle of bubble dynamics for the iron oxide took similarly about 1.0 ms. The cycle periods after the first cycle varies from 1.0 to 2.0 ms, since these periods strongly depend on the subsequent fine fragmentation process.

2.3.4 Stratified Liquid-Liquid Mixing

As discussed in the previous section, the local explosion of a molten drop in highly subcooled water results in fine fragmentation along the droplet surface induced by the stratified explosion. To estimate the amount of melt fragments participated during the stratified explosion, the mixing depth is estimated in a case shown in Figure 2.13 in which a melt drop is covered by vapor film and Rayleigh-Talyor (RT) instability is developed in liquid-vapor interface due to the pressure impulse. This model for the mixing depth during the stratified explosion in the stratified geometry was originally developed by Bang and Corradini.

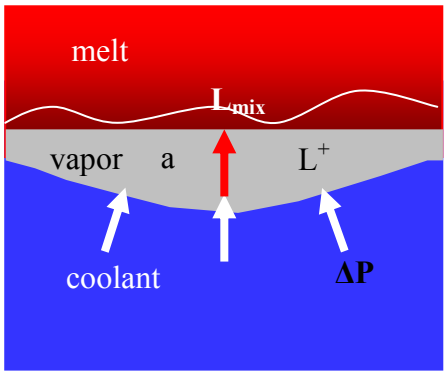

Figure 2.13: Schematic of stratified mixing model.

The mixing depth during the stratified explosion in a geometry as shown in Figure 2.13, L_{mix}, due to RT instability can be defined as,

$$L_{mix} = u_{mix}\tau_{mix} \tag{2.10}$$

where u_{mix} is the initial mixing velocity and τ_{mix} is the mixing time. The mixing velocity can be estimated from Bernoulli's equation for invicid fluid as below,

$$u_{mix} = \frac{u_{jet}}{1+\sqrt{\frac{\rho_m}{\rho_l}}} \tag{2.11}$$

where u_{jet} is the initial jet velocity due to the pressure difference in the liquid-vapor interface induced by RT instability, ρ_m is the melt density and ρ_l is the coolant density. The mixing time can be associated with the fastest growing wavelength, n, induced by the RT instability. Therefore the mixing time can be given as,

$$\tau_{mix} \cong \frac{1}{n}\sqrt{\frac{\rho_m}{\rho_l}}$$
$$\text{where } n = \left[\left(\frac{4}{27}\right)\frac{a^3(\rho_l-\rho_v)^3}{\sigma(\rho_l-\rho_v)^2}\right]^{1/4} \tag{2.12}$$

Now, the jet velocity can be obtained from the instability acceleration, a, and acceleration time τ_{ac},

$$u_{jet} = a\tau_{ac} \text{ where } a = \frac{\Delta P}{\rho_l L^+} \text{ and } \tau_{ac} = \frac{2L_c}{u_c} \tag{2.13}$$

where ΔP is the pressure difference (=P-P_∞), L_c is the characteristic length of interface instability acceleration and u_c is the mixture sound velocity. The characteristic length, L^+, can be a curvature (wavelength) of interface as given below,

$$L^+ \cong \lambda_{RT} = 2\pi\sqrt{\frac{\sigma}{g(\rho_l - \rho_v)}} \tag{2.14}$$

where σ is the surface tension and g is the gravitational acceleration. Finally, the mixing depth during the stratified explosion can be expressed as

$$L_{mix} = \frac{\left(\frac{\Delta P}{\rho_l L^+}\right)\left(\frac{2L_c}{u_c}\right)}{\left(1+\sqrt{\frac{\rho_l}{\rho_m}}\right)}\left[\left(\frac{4}{27}\right)\frac{a^3(\rho_l - \rho_v)^3}{\sigma(\rho_l - \rho_v)^2}\right]^{-1/4} \tag{2.15}$$

Form equation (15), the mixing depth with respect to the external pressure is evaluated by taking u_c=50 m/s and L=5 mm for the present tests as shown in Figure 2.14. Figure 2.14 indicates that the mixing depth increases with the imposed external trigger pressure. At the external trigger pressure of approximately 1.0 MPa for the present tests, the mixing depth of approximately 0.35 mm can be estimated. By assuming that the local explosion propagates over the entire surface of the droplet with this mixing depth, approximately 20 % of the total mass of the molten drop is fragmented during the stratified explosion. In this figure, mixing depths for other materials by considering their physical properties. This preliminary analysis can be verified with our quantified X-ray image data similarly shown in Figure 2.15 in near future.

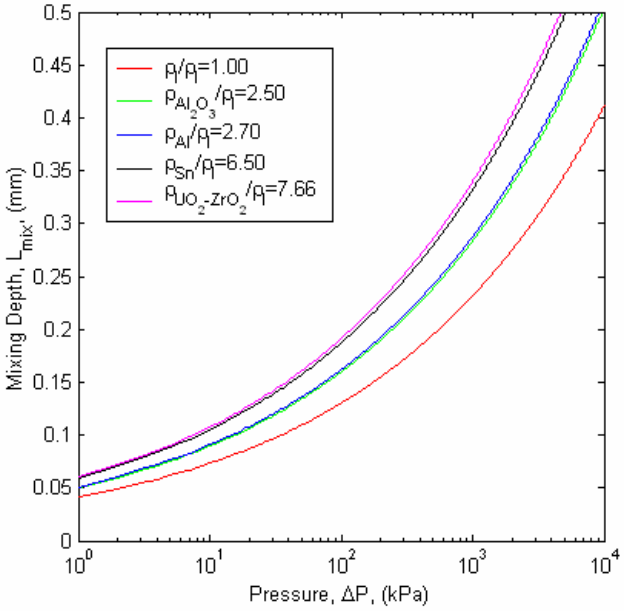

Figure 2.14: Mixing depth during stratified explosion on single drop with different materials

2.3.5 Distribution of Finely Fragmented Melt Particles

Figure 2.15 shows the original, processed and calibrated X-ray radiographs at 22 ^{o}C water. The thickness of the melt fragment distribution is calibrated as mentioned in the previous section. The calibrated thickness of the melt fragments shown in this figure is, in fact, the cumulative mass of fragmented melts along the line of the incident X-ray beam. From the images in this figure, at τ=0, the thickness of the melt drop prior to the explosion is about 5~6 mm at the center of the drop and 1~2 mm near the edge of the drop. When the drop is triggered and expanded, the shell of the fragmented particles

accumulating in the interface becomes thicker, from 1~2 mm to 3~4 mm. The hollows inside the shell formed after the explosions have about 1mm thick of fragmented particles. The calibrated images, however, still have significant random noises which create unrealistically fluctuating values of the melt thickness. For the accurate quantification of the melt distribution, the acquisition of quality images and the development of advanced image processing techniques should be needed.

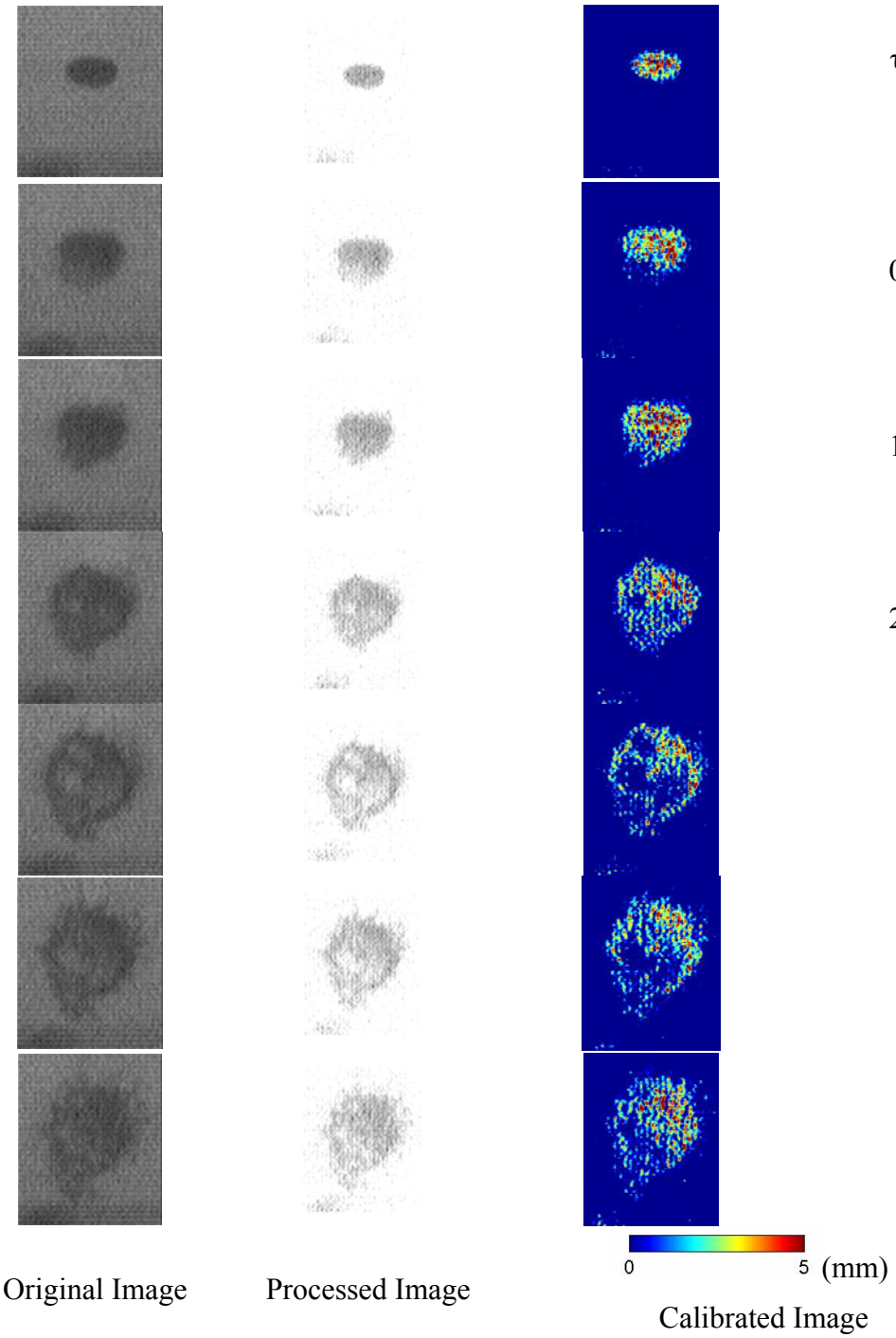

Figure 2.15: X-ray radiographs (right) of the vapor explosion of 0.7g tin drops at 1000 ^{o}C in 22 ^{o}C Water. Image size for the original radiographs is 29.3x24.6mm (199x167 pixels).

2.4 SUMMARY

In year 2003, experimental efforts on the vapor explosions were concentrated on identification of the fine fragmentation process during steam explosion employing high-speed continuous X-ray radiography. Single drop steam explosion experiments were performed with 0.7g molten tin drops at 600~1100 ^{o}C in various subcooled water. Observations were conducted by using the continuous high-speed X-ray radiography and photography. For the first time, transient fine fragmentation process of a melt drop during steam explosion was quantified.

The high-speed X-ray images revealed the internal dynamic structures of the molten drop during the vapor explosion process, i.e., triggering, propagation and expansion of the drop and fragments in small-scale. For highly subcooled water, the images showed that the small-scale stratified explosion initiated at the circumference or lower hemispherical region of an ellipsoidal or spherical droplet and propagated along the melt surface. An analysis of the estimation of the mixing length in this stratified explosion indicated that approximately 20% of the total mass of the molten droplet was fragmented. During the fragments expansion process, a shell of fragmented melt particles at the boundary was identified.

For lower subcooled water, the vapor/gas pocket formed during the impingement of molten tin drop into water and film boiling heat transfer in water provide an extra triggering source. The maximum expansion diameter of fragmented particles and vapor bubble reached 3~3.5 times the initial diameters. X-ray radiographic images showed a shell of fragmented melt particle near the vapor bubble boundary during the explosions.

Future tests will focus on X-ray radiography to quantify the multiphase parameters such as phase volume fractions with other metallic melts as well as various single and binary oxide melts.

3. SINGLE DROP STEAM EXPLOSION: QUENCHING BOILING

3.1 INTRODUCTION

In single drop steam explosion, the precise estimation of thermal conditions of the melt droplet prior to triggering of explosion is also needed to evaluate the triggering process of the explosion. In so doing, a simple quenching experiment which employed a stainless steel ball which was heated up to more than 1000 ^{o}C and dropped into coolant at various subcooling. The data measured in the experiments will be used to develop a theoretical model for the quenching process of a melt droplet which includes direct contact boiling and film boiling heat transfer.

3.2 EXPERIMENT

Quenching experiment of a stainless steel spherical ball was conducted in a pool of different liquids. The study includes low degrees of subcooling and highly subcooled distilled water used to cool the heated sphere plunged at higher temperature. Two different size spherical SKF bearing balls, RB-10/G20W and RB-20/G20W, with sizes of 10mm and 20mm in diameter respectively, were used in the experiments. The sphere is chosen due to its geometry which represents a single molten drop in modelling. The other advantages of selecting a spherical geometry are: the uncounted heat does not pose any problem. Therefore it is ensured that all the heat from the heated sphere is transferred to the surrounding liquid.

3.2.1 Description of experiment apparatus

The experiment set up involved different apparatuses, such as: heating furnace, sphere and its support system, Argon system, pneumatic cylinder, test vessel, data acquisition system, video camera, high speed camera, motion scope and thermocouples. A very brief description of the their contribution and concurrence in the test will be presented for the main apparatuses.

To support a stable film on a heated sphere in highly subcooled liquid requires higher initial temperature of the sphere. However, the possibility of getting to a higher initial temperature through the conventional way of heating is unlikely. In this experiment, this is achieved by using an induction heating, which is capable to heat the sphere to a higher temperature. The induction furnace used is able to supply up to 6 KW power within a short period of times.

The test section is a 10 cm x 10 cm rectangular vessel having depth of 15 cm. It is made of Plexiglas, for visual observation from the outside and videotaping. Two holes on opposite side of the test section was drilled, one is to put in a K-type thermocouple in to the liquid pool for regulating its temperature. It is positioned in a way that the average temperature of the bulk liquid could be recorded. The other one was to plug a pressure transducer that will be in the use to measure peak pressures, which takes place when the vapour film collapsed. The liquid is filled to 12 cm height of the vessel and the sphere is dipped to a depth of during the experiment.

The thermocouple stem was arranged to support the sphere, this way the heat loss from the support system will be minimised. The thermocouple inserted in the sphere, besides

supporting the sphere its main task is to acquire the transient cooling temperature history of the centre of the sphere.

Hole was drilled on the sphere in the centreline up to half the diameter and the sheathed thermocouple was then inserted. Only one thermocouple for each sphere was applied, again not to loose heat through the support system. For the smaller sphere (10mm diameter), a very thin, 0.5mm OD and 305 mm long, K-Type Inconnel sheathed ungrounded thermocouple (KMQIN-020U-12), was used. This is then put in to a 0.9mm OD still tube, fixed at the other end of the thermocouple. Roughly, 40mm from the sphere, the tube is reinforced by another steel tube 3.1 mm OD. In the case of the larger sphere (20mm diameter), stainless steel sheathed, ungrounded K-type thermocouple (1,5mm OD and 305 mm long) (KMQSS-062U-12) is used. The thermocouple stem is reinforced by a steel tube 4mm OD 47mm from the sphere, The attachment of the thermocouple to the sphere has been thought of too much, the likely means were soldering, welding on the outside, and friction joint. Here friction joint is utilized.

The sphere support system is fixed to the end of a piston rod. A pneumatic double acting cylinder with bore diameter ϕ 20mm and Stroke 160mm long, that can handle a maximum of 10 bar actuates the rod. Pressurized argon cylinders were used to operate the cylinder and the system pressure of the argon is varied to control the speed of the ball.

Transient tests are conducted and LabView program and processor via centrally located thermocouple and the thermocuple inserted to the test vessel continually measures the centre temperature of the sphere and the liquid bulk temperature, respectively.
The thermocouple wires are plugged in to A National Instrument A-D Converter and amplified to and the data is fed in to a Compaq Computer connected to it. The data sampling is 100-250 Scans per second. The data taking frequency is too fast compare with the thermocouple response time. A high-speed camera and Video is employed to view the configuration of the film and process the image.

The observations of the film are showed in the Figure 3.1

Figure 3.1: Vapor film boiling over a 10mm sphere at the subcooling of 80 K

3.3 DATA ANALYSIS

A stainless steel sphere heated to a higher temperature (800-1100 ^{o}C) is quenched in subcooled distilled water, degree of subcooling ranging 10 to 80 ^{o}C. The transient temperature of the center of the sphere is recorded through all the boiling regions using a DAS. In the preliminary data reduction a lumped capacitance method is used to calculate the surface heat flux. The Biot number calculated in the film boiling region is less than the minimum required to assume lumped capacitance i.e., 0.4. However this assumption is not always true, thus the use of Inverse heat conduction problem is under way. The temperature history of the center of the sphere is presented in the Figure 3.2.

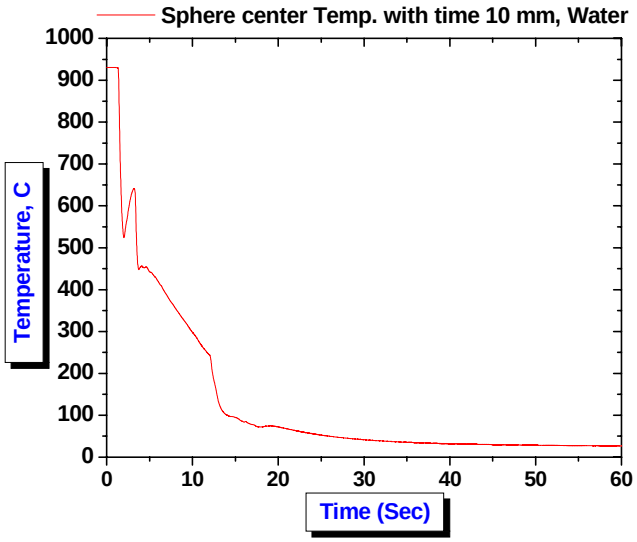

Figure 3.2: Center temperature of a 10mm sphere at the subcooling of 80 K

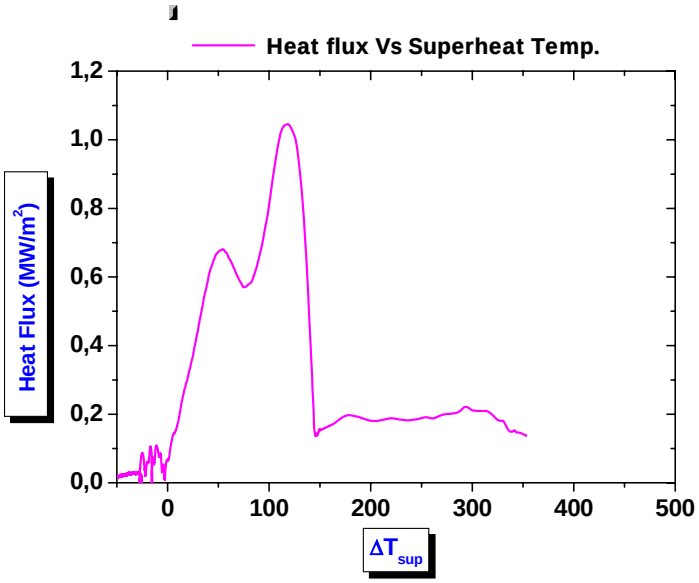

Figure 3.3: Heat Flux of a 10mm sphere during the quenching at the subcooling of 80 K

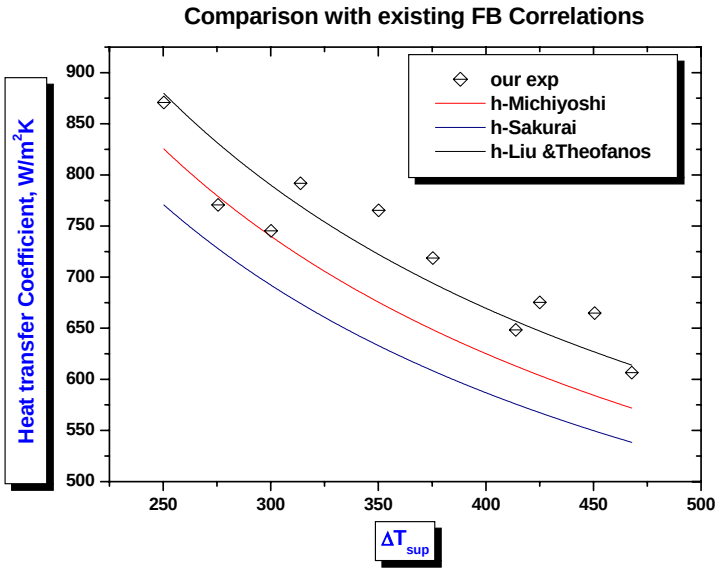

Figure 3.4: Film boiling heat transfer coefficient of a 10mm sphere during the quenching at the subcooling of 80 K

3.4 SUMMARY

The heat transfer coefficients obtained from the experiments are compared with the known correlations developed so far. The comparison showed that the experiment methodology is in the right pattern and assumption of lumped parameter for the film boiling region show little effect on the result. These are shown in Figures 3.3 and 3.4.

A theoretical model that considers the neglected assumptions in earlier works is under development. The fundamental equations and Differential equations are already developed. In the future a numerical solution of the model will be completed and verified with the experimental database.

4. SINGLE DROP STEAM EXPLOSION: BUBBLE DYNAMICS

4.1 INTRODUCTION

When two liquids, one at a very high temperature and another at a low temperature come into contact, rapid heat transfer can occur between the two liquids. If the boiling point of the liquid at low temperature is much lower than the temperature of the high temperature liquid, then vapors forms around the high temperature liquid. If the vapor generation due to the two liquids interaction is so rapid that the accompanying pressurization cannot be relieved in the event time scale, a shock wave will be formed in the mixture. Steam explosions have been observed in the metal industry, paper industry, in the interaction between hot volcanic lava and water. They could also occur in the postulated core melt accident scenarios in nuclear industry. In this paper, an attempt to explain the single drop experiment on steam explosion using molten iron oxide as a hot drop in water under a pressure pulse produced by exploding wire as reported in Nelson et al [2] is made.

In 1978 Sharon and Bankoff and almost simultaneously Patel and Theofanous proposed a fragmentation model based on the Taylor instability and boundary layer stripping caused by intensive slip flow around the drop, following the traveling of a shock pressure in the two phase coarse mixture of melt and coolant. However this model may not be a suitable one to predict single drop experiment performed by Nelson et al., where trigger pressure amplitude was not that significant to cause intensive slip flow around the drop. It is point out here fine fragmentation and then vapor explosion were observed under a relatively low pressure pulse generated by the exploding wire.

Buchanan has proposed a model of a single drop fuel coolant interaction which is caused by rapid increase of interaction area due to penetration of a coolant micro jet into the hot molten fuel and turbulent mixing caused by the high speed jet. Generation of micro jet flow during asymmetrical collapse of a vapor bubble on the hot surface was initially analyzed by Plesset and Chapman. However it is not clear whether micro jets can be formed or not during collapse of a thin vapor film around a hot droplet.

A mechanism, similar to the one described by Buchanan, is proposed by Kim and Corradini where an array of micro jets is assumed to form by Taylor instability of vapor-liquid interface during the collapse phase of vapor film. Micro jets formed thus penetrate, entrap in the hot drop, vaporize and expand, which then joins together to form a vapor cell within the melt. Finally this vapor cell breaks the outer shell of the melt droplet to form a mixture of melt, coolant and vapor, which then grows by repeating the procedure. However the agreement between numerical calculations with experimental results is not found to be very satisfactory. A simplified model, based on the vapor bubble dynamics and Taylor instability, is proposed by Inoue et al., which finds good agreement between the experimental results with the numerical one, but the amount of fragmented mass in each vapor bubble collapse is assumed to follow the experimental data.

So it is necessary to look the existing models in order to better predicting the existing experimental results. An analytical model similar to the one proposed by Inoue et al. has been remodeled by including a stability model for the purpose of analyzing fragmentation process; this has been compared with Nelson et al. single drop

experiment. Stability analysis considered here is similar to one described by Kim and Coradini, but many more features which have been neglected by Kim and Coradini have been included. We shall see in results and discussions section that inclusion of the extra feature result changes lot in terms of mode of instabilities are concerned.

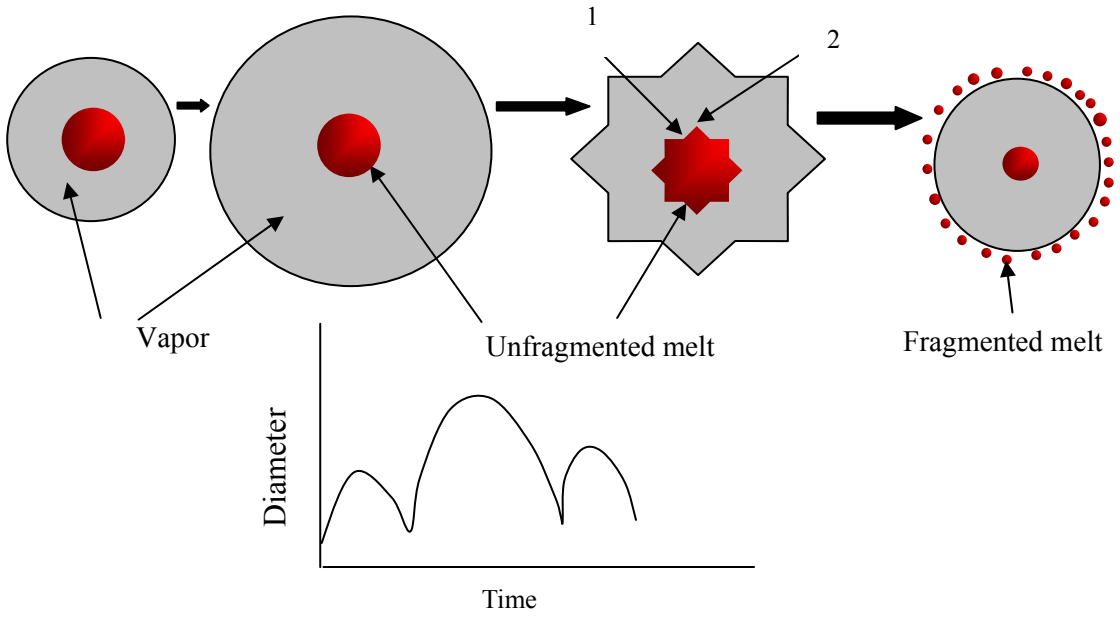

Figure 4.1: Physical Model

4.2 PHYSICAL MODEL

Steam explosion phenomena described here are based primarily on the ideas proposed by Inoue et al. Basic idea is that film boiling generates vapor surrounding the hot fluid. This vapor film behaves like a bubble and undergoes collapse. Due to the collapse of vapor film, spherical instability develops in both vapor film as well as the melt. During the collapse process very large pressure is generated within the bubble, which essentially squeezes the melt, and this in turn develops similar spherical instability in the melt drop. There is no straightforward relation by which exact amplitude of spherical instability mode of the melt can be estimated. In the present study, assumption is made that the amplitude of the spherical instability of the melt drop is proportional to the amplitude of the vapor film surface instability.

We assume that instability amplitude of the melt is being removed from the melt to form finer spherical particle whose dimension corresponds to the wavelength of instability. These fine particles undergo film boiling under a pressure pulse generated due to bubble collapse. The instability model considered here is somewhat similar to the one consider by Kim and Corradini. However additional terms due to viscous effect are considered in the present model. Actually the instability model closely matches the study made in sonoluminescence by Brennen et al. It should be mentioned that during the collapse phase of the bubble the instability grows. As a result, pressures at point 1 & at point 2 (See. Figure 4.1) are different. At point 1 pressure is higher than that at point 2. So due to the pressure difference, finger like melt is removed from the main mass to fly off towards the boundary. This removed mass produces more steam which is added to the

main mass of vapor bubble. Vapor bubble grows and pressure drops inside the bubble. Due to the inertia and surface tension, bubble motion reduces and bubble reaches its maximum dimension. Then, bubble suddenly collapses and process repeats itself. We assume in the calculation that fly-off mass does not contribute to the next cycle.

4.3 MATHEMATICAL FORMULATION

Following Inoue *et al.*, we assume the following: (1) temperature in the fine particle is considered uniform because of its small size and (2) pressure and temperature in the vapour phase are uniform during the growth and collapse of the bubble. However, unlike Inoue *et al*., we assume temperature variation for the un-fragmented mass. We consider heat transfer from the parent melt, which was not considered by Inoue *et al*.

The growth and collapse of vapor bubble is assumed to follow the classical Rayleigh-Plesset equation with some modification of mass transfer due to evaporation and condensation. Modification on the mass (steam) transfer terms due to condensation and evaporation is considered in the bubble dynamics equation (1), since the bubble dynamics here is dominated by the evaporation and condensation of water vapor. This has not been given much importance in the earlier literatures related to steam explosion phenomena. The detailed derivation of the equation (1) can be seen in Yasui, which is written as follows:

$$\begin{aligned}
&\left(1-\frac{\dot{R}}{C_\infty}+\frac{\dot{m}}{C_\infty\rho_{L,i}}\right)R\ddot{R}+\frac{3}{2}\dot{R}^2\left(1-\frac{\dot{R}}{3C_\infty}+\frac{2\dot{m}}{3C_\infty\rho_{L,i}}\right)\\
&=\frac{1}{\rho_{l,\infty}}\left(1+\frac{\dot{R}}{C_\infty}+\frac{R}{C_\infty\rho_{L,\infty}}\frac{d}{dt}\right)\left[P_B-P_S(t)-P_\infty\right]\\
&+\frac{\dot{m}R}{\rho_{L,i}}\left(1-\frac{\dot{R}}{C_\infty}+\frac{\dot{m}}{C_\infty\rho_{L,\infty}}\right)\\
&+\frac{\dot{m}}{\rho_{L,i}}\left(\dot{R}+\frac{\dot{m}}{2\rho_{L,i}}+\frac{\dot{m}\dot{R}}{2C_\infty\rho_{L,i}}-\frac{R}{\rho_{L,i}}\frac{d\rho_{L,i}}{dt}-\frac{\dot{m}R}{C_\infty\rho_{L,i}^2}\right)
\end{aligned} \tag{4.1}$$

where, the dot denotes the times derivative (*d/dt*), C_∞ is the sound speed in the liquid at infinity, $\rho_{L,i}(\rho_{L,\infty})$ is the liquid density at the bubble wall (at infinity), $P_B(t)$ is the liquid pressure on the external side of the bubble wall, $P_s(t)$ is the trigger pressure in the present case and P_∞ is the undisturbed pressure. P_B is related to the pressure inside the bubble ($P_g(t)$) by equation (4.2).

$$P_B(t)=P_g(t)-\frac{2\sigma}{R}-\frac{4\mu}{R}\left(\dot{R}-\frac{\dot{m}}{\rho_{L,i}}\right)-\dot{m}^2\left(\frac{1}{\rho_{l,i}}-\frac{1}{\rho_g}\right) \tag{4.2}$$

where σ is the surface tension, μ is the liquid viscosity, and ρ_g is the vapor density inside the bubble. In the equation (2), vapor is assumed to follow van der Walls equation of state, which is expressed as

$$\left[P_V(t)+a\rho_V^2\right]\left(\frac{1}{\rho_V}-b\right)=R_V T_V \tag{4.3}$$

where a, b and R_g are the three constants, whose values are considered as 1708.34 Pa-m^6/kg^2, 1.694x10^{-3} m^3/kg and 460 J/kg-K respectively. Equation (4.1) is completed with initial conditions, which can be written as $R(0)=R_0$, $\dot{R}(0)=\dot{R}_0$, $P_V(0)=P_{V0}$ and $T_V=T_{V0}$. Temperature inside the bubble is calculated by solving the equation (4.4), which is expressed as

$$T_V = \frac{E_V}{M_V C_{VV}} \tag{4.4}$$

where E_V, M_V and C_{VV} are the internal energy, mass and specific heat of vapor at constant volume respectively. We considered variable C_{VV}, for the calculation of vapor temperature. The change of internal energy of the bubble can written as follows

$$\begin{aligned}\Delta E(t) = {} & 4\pi R^2 \dot{R}\left(-P_g(t) + \dot{m}_{eva}\int_0^{T_I} C_{PV}dT\right) \\ & - 4\pi R^2 \dot{R}\left(\dot{m}_{con}\int_0^{T_V} C_{PV}dT - h_m(T_m - T_\infty)\right) \\ & + m_v \int_0^{T_I} C_{PV}dT\end{aligned} \tag{4.5}$$

where T_I and T_m are calculated from the interface and melt temperature respectively. C_{pv}, and $\dot{m}_{eva}$ ($\dot{m}_{con}$) are the specific heat at constant pressure and the rate of evaporation (condensation) respectively. Variable C_{PV} is considered in the calculation. 'h_m' and 'm_v' are the convective heat transfer coefficient and the vapor generation rate due to the fragmented mass respectively. In the energy equation (4.5) of vapor, we considered additional heat transfer from the parent melt to vapor, which was ignored by Inoue *et al*. In fact, we are motivated to use this term according to Prof. Inoue's suggestion through our private communication.

Interface temperature in equation (4.5) is calculated from energy balance at the interface of vapor and water, which takes the form of equation (4.6):

$$T_I = T_\infty - \sqrt{\frac{D_l}{\pi}}\int_0^u \frac{q_\ell}{K_\ell R^2\sqrt{(u-v)}}dv \tag{4.6}$$

where $u = \int_0^t R^4 dt$ and $v = \int_\theta^t R^4 dt$. Fragmented melt temperature is calculated from the energy balance of the fragmented mass, which can be written in the form of equation (7) below:

$$C_{vm}\dot{T}_{mf} = -S_{mf}h_{mf}(T_{mf} - T_\infty) \tag{4.7}$$

Initially, un-fragmented melt temperature, T_m, is considered as T_{mf}. In equation (4.7), S_{mf} and h_{mf} are the surface area and convective heat transfer coefficient of the fragmented particles. Fragmented particle is assumed to take the shape of a sphere. The variation of un-fragmented melt temperature is assumed to follow the equation (4.8) as

$$C_{vm}\dot{T}_m = -S_m h_m(T_m - T_\infty) \tag{4.8}$$

It is very difficult to find a suitable heat transfer coefficient under a pressure pulse especially one that can arise in this type of scenarios. Some results of heat transfer coefficient under pressure pulse are available from a heated platinum foil, but implementation of those types of heat transfer coefficient in present case is very complicated. In the present case, we considered the average heat transfer coefficient

during the pressure pulse. Maximum average value of heat transfer coefficient is around 2.5 kW/m^2-K, in Inoue *et al.*. This value is attained when the pressure pulse amplitude $(P_V - P_\infty)$ is above 2 bar. When the surrounding the liquid pressure is below 1.5 bar, normal heat transfer correlation for forced convection for spherical particle is used, which can be expressed as

$$\frac{Nu}{1+2/Nu} = H(Fr, d^{'})K(d^{'})\left[\left(\frac{Ar}{Sp^{'}}\right)M_c\right]^{0.25} \tag{4.9}$$

In the above equation Nu is the Nusselt number which is equal to $h_m d / k_m$. From the equation (4.9), h_m can be calculated. H and K are the two constants for forced convection and diameter of the particles respectively. $Ar, d^{'}, Sp^{'}$ and M_c are four numbers. Details of the discussions on these can be seen in Liu and Theofanous. H is a function of Froude (Fr) number, which depends on the fluid velocity or the particle velocity. In the present case, unfragmented mass is considered to have a velocity of ~0.5 m/sec, while fragmented particle is assumed to have a velocity, which is same as the velocity of the bubble wall. It may be entirely possible to consider the equation (4.9) for the whole bubble process, but it is yet to be tested. In equation (4.5), m_v is calculated from the energy of fragmented particles. Energy balance of the fragmented particles can be written in mathematical form as,

$$\dot{m}_v = \frac{1}{L}\left[h_{fm}(T_{fm} - T_\infty) - q_\ell\right]\frac{S_{fm}\Delta M_m}{\rho_{fm}} \tag{4.10}$$

q_ℓ in the above equation is estimated by the following equation as

$$q_l = (m_{con} - m_{eva})\left[L + \int_{T_V}^{T_I} C_{PV}\, dT\right] \tag{4.11}$$

where

$$m_{con} = \alpha\sqrt{\frac{M_0}{2\pi R_0 T_V}}P_v \tag{4.12}$$

and

$$m_{eva} = \alpha\sqrt{\frac{M_0}{2\pi R_0 T_I}}P_I \tag{4.13}$$

In the equations (4.12) and (4.13) α is the evaporation (condensation) coefficient. In the literatures, different evaporation (condensation) coefficients are considered. In this calculation, the value of α is taken as 0.04. Surface area per unit volume (S_m or S_{mf}), in the equations (4.7) and (4.8), has been calculated from the parent melt diameter (d_m) and fragmented melt diameter (d_{mf}). In general surface area per unit volume (S) for a spherical particle is expressed as,

$$S = \frac{6}{d} \tag{4.14}$$

Size of the fragmented particle (d_{mf}) is considered to be the one, which is equivalent to the most unstable wavelength corresponding to the Rayleigh-Taylor instability. This wavelength mode is estimated from the non-linear stability analysis of Rayleigh-Plesset equation (4.1) of the vapour bubble, which will be discussed in the following section.

4.4 STABILITY ANALYSIS

Bubble in the collapse phase is vulnerable to instability especially the one of the type of Rayleigh-Taylor instability. A theoretical formulation of the spherical stability of bubble including viscous effects was presented in Prosperetti. A very similar formulation was assumed by Kim and Coradini. The present formulation covered many more features in the stability analysis, which was not given importance in the model developed by Kim and Coradini. This has impact in the stability mode of the bubble dynamics. The result is based on a linear analysis according to which bubble shape is perturbed to $r = R(t) + a_n(t)Y_n^m(\theta,\phi)$, where R is the instantaneous bubble mean radius, Y_n^m a surface harmonic, and a_n the amplitude of the surface distortion. Since, in the linear regime, the dynamics of the perturbation is independent of the index '*m*', we drop it in the following. It is found that a_n satisfies the following equation:

$$\begin{aligned}
&\ddot{a}_n + \left[3\frac{\dot{R}}{R} + 2(n+2)(2n+1)\frac{\nu}{R^2}\right]\dot{a}_n \\
&+ (n-1)\left[-\frac{\ddot{R}}{R} + (n+1)(n+2)\frac{\sigma}{\rho R^3} + 2(n+2)\frac{\nu\dot{R}}{R^3}\right]a_n \\
&+ n(n+1)\frac{\dot{R}}{R^2}\int_{R(t)}^{\infty}\left(\frac{R^3}{r^3} - 1\right)\frac{R^n}{r^n}U(r,t)ds \\
&- 2n(n+1)(n+2)\frac{\nu}{R^3}\int_{R(t)}^{\infty}\frac{R^n}{r^n}U(r,t) = 0
\end{aligned} \tag{4.15}$$

Here dots denote time derivatives and ν, and ρ and σ are, respectively, the kinematic viscosity, density, and surface tension coefficient of the liquid. The field $U(r,t)$, the toroidal component of the liquid vorticity, satisfies

$$\frac{\partial U}{\partial t} + \frac{\partial}{dr}\left(\frac{R^2}{r^2}\dot{R}U\right) = \nu\frac{\partial^2 U}{\partial r^2} - n(n+1)\frac{\nu}{r^2}U, \tag{4.16}$$

subject, at $r=R(t)$, to boundary condition

$$\begin{aligned}
&U(R(t),t) + 2R^{n-1}\int_{R(t)}^{\infty} r^{-n}U(r,t)dr = \\
&\frac{2}{n+1}\left[(n+2)\dot{a}_n - (n-1)\frac{\dot{R}}{R}a_n\right].
\end{aligned} \tag{4.17}$$

The physical reason for this rather complicated mathematical structure of the problem is that both the amount of vorticity generated at the bubble surface and viscous damping of the shape oscillations depend on the instantaneous distribution of vorticity. The spatial integrals of the field U are necessary to properly account for this instantaneous distribution. With a boundary layer type of approximation, equation (4.15) can be written as

$$\ddot{a}_n + \left[\begin{array}{l} 3\dfrac{\dot{R}}{R} + 2(n+2)(2n+1)\dfrac{\nu}{R^2} + \\ 2\dfrac{n(n+2)^2}{1+2\delta/R}\dfrac{\mu}{\rho_{L\infty}R^2} \end{array} \right] \dot{a}_n$$

$$+ (n-1)\left[\begin{array}{l} -\dfrac{\ddot{R}}{R} + (n+1)(n+2)\dfrac{\sigma}{\rho R^3} + \\ 2(n+2)\dfrac{\nu\dot{R}}{R^3} + \\ 2\dfrac{\nu\dot{R}}{R^3}\left((n+1)(n+2) - \dfrac{n(n+2)}{1+2\delta/R} \right) \end{array} \right] a_n = 0 \qquad (4.18)$$

where δ is the boundary layer thickness. Brenner *et al.* proposed to define this quantity as

$$\delta = \min\left(\sqrt{\frac{\nu}{w}}, \frac{R}{2n} \right) \qquad (4.19)$$

in which w is the frequency of the sound driving the radial oscillations. The quantity $R/2n$ acts as a cutoff justified on the basis of a quasi-static argument for small bubble. However, it will be more accurate to solve full equations (4.16) and (4.17) in the liquid phase. In the present calculation, we considered the approximations suggested by Brenner *et al*. As, there was no continuous sound field 'ν/w', term has been omitted in the calculations. It can be seen later that it can predict the fragmented mass reasonably well within the limitation of this approximations. More ambitious attempt to calculate the accurate vorticity generation in the liquid phase for a large number of modes using the equations (4.15) and (4.16), will be postponed to a future study. Here, we are mainly interested to find the suitability of its use in the steam explosion problem for predicting the transient fragmentation process.

4.5 RESULTS

The above equations (4.1)-(4.19) are non-linear. In the present case, the well-known fourth order Runge-Kutta method is used to solve these equations. Parameters used in the calculation are presented in the Table 4.1. These values are the conditions of Nelson *et al.* experiment. In the calculation, initial bubble radius, velocity, vapor pressure and its temperature are taken as 0.0022 mm, 0 m/sec, 1×10^5 Pa and 375 K respectively. The reason for using ambient pressure arises from that in the Nelson's data, there is no high pressure at the start of the experiment except the imposed pressure pulse. Further, we would like to add that to maintain the equilibrium with ambient pressure, vapor pressure is expected to be close to the ambient pressure. Initial temperature of the vapor is assumed to be the saturated water temperature. In the calculation, we considered zero initial bubble wall velocity. In addition, it should be mentioned here that Inoue used different conditions for their calculation. In our calculation, we used ambient pressure to be 1 bar, which is slightly different from the Nelson's experiment. However we believe that qualitative behavior of this phenomenon would be unaffected.

Table 4.1. Calculation conditions

Temperature of molten iron oxide, K	2230
Mass of molten drop, g	0.0546
Diameter of molten iron drop, mm	2.78
Initial sub-cooling of liquid, K	71
Initial pressure, MPa	0.1
Peak triggering pulse, MPa	0.71
Liquid	Water

Using the equation (4.18), vapor bubble stability is analyzed. Solution procedure to calculate the equation (18) can be seen in Hilgenfeldt *et al*. We followed an approach similar to that of Hilgenfeldt *et al*. In general, Rayleigh-Taylor instability occurs during the collapse and rebound phase of the bubble dynamics. In the present case, if the amplitude of any mode is larger than the thickness of vapor shell, then bubble is considered unstable. This, we used as a criteria for the stability.

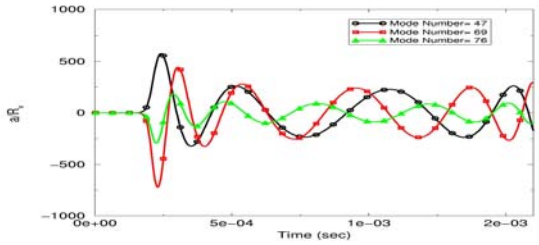

Figure 4.2: Development of shape instability of various modes after the start of the bubble dynamics process.

We analyzed ~200 modes to find out the potential unstable modes. In the calculation, we assumed that outer shell of the melt is also oscillating proportionally with the oscillations of the bubble surface. This may not be when pressure inside the bubble is not significant. But at the higher pressure, this should be plausible. In the critical condition of stability, a shell of melt (equivalent to the amplitude of oscillation) is removed from the original mass of melt. Removed mass forms a number of finer particles, whose diameter is the wavelength of oscillation. Those finer particles come to the surface of bubble and generate vapor, which is added to the main mass of the bubble. So how much melt will be removed from the parent melt is decided by the instability mechanism. This is one of the major deviations from the calculation of Inuoe, who estimated the fragmented mass to match the bubble dynamics observed experimentally. In the present calculation, fragmented mass is a result of the stability analysis.

Figure 4.3: Development of shape instability for various modes after 1.6 ms.

To solve the equation (4.18), one needs the initial amplitude. In the calculation, we assumed the amplitude of oscillation is around 0.05% of the initial radius. However, we believe that initial amplitude is not so important, since growth rate of the amplitude of instability mode is very high. What we find is that bubble becomes unstable during the late phase of its collapse and the early phase of its growth. Various stability modes are shown in the Figures. (4.2), (4.3) and (4.4). From the figures, it may be realized that different modes can be activated in different experiments, as they have almost equal potential. Depending on the mode of instability, these can give different bubble dynamics for same initial conditions.

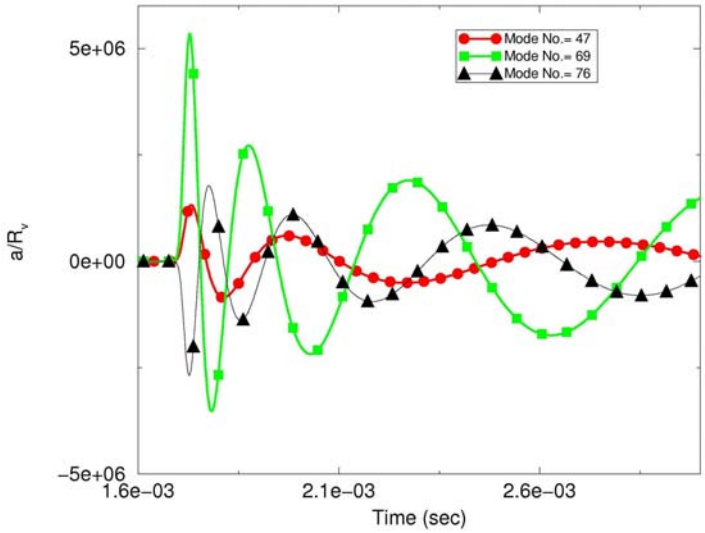

Figure 4.4: Development of shape instability for various modes after 3 ms.

A typical bubble dynamics obtained thus is shown in Figure (4.5) for the instability mode of 76. Qualitative agreement between experimental bubble dynamics and numerically obtained bubble dynamics is very good. Now, if we assume that fine particles are produced due to the instability mode 76, then wavelength of instability is ~114 μm. Assuming that the particles are spherical and their diameter is of the order of wavelength, we find that it is within the range of experimentally obtained diameters. We feel that the particles formed form a vapor cell around them and undergo similar growth and collapse like parent one. Collapse of the smaller bubble occurs when a pressure pulse is generated due to the parent bubble collapse. Thus much smaller particles are possible, from the initially formed particles. Similar bubble dynamics are obtained using different instability mode.

The parameters used in the calculations gave an estimate of the fragmented melt mass of the order of ~ 15-25% of the original mass in the first collapse. In the second collapse, fragmented mass varies from 75 - 85% of the rest of the mass. However we did not find any fragmentation to occur in the third collapse. We should point out here that growth rate of various modes are pretty high after the second collapse, so stability analysis suggests that vapor bubble is unstable during maximum radius region, which does not serve any purpose. So, we initialized the amplitude of all modes of instability to the initial value and also we suppressed the velocity of the all the modes to near zero and, then allowed the stability mode to grow naturally, as we did initially. Unlike Inoue *et al.*, bubble does not collapse perfectly, but re-bounds from the minimum and generates a

pressure pulse. It may so happen, that we need to trigger a pressure pulse, as is the case of Nelson's experiment. However, this has not been tested in the calculations.

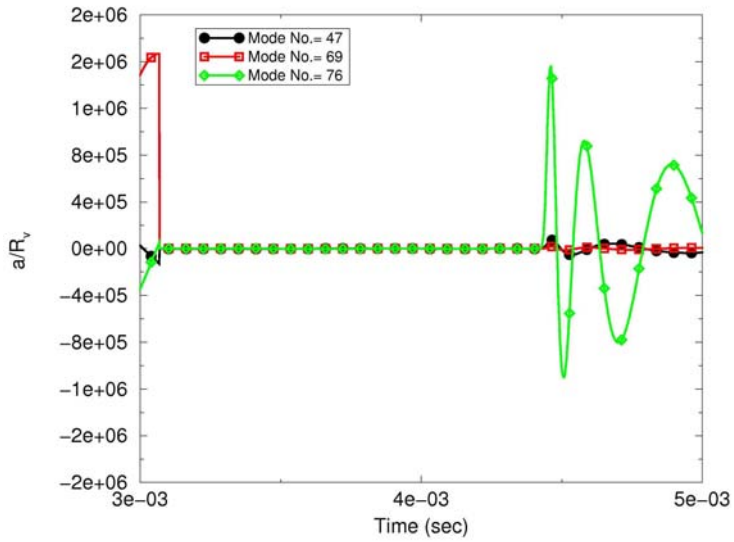

Figure 4.5: Time history of Bubble Radius.

Vapor pressure history is shown in the Figure (4.6). Similar to experiment, stronger pressure pulse is observed in third collapse of the bubble. However, amplitude of pressure pulse is higher than the experimentally observed one. Experimentally observed pressure pulse was recorded far away from the bubble, whereas this vapor pressure can be observed near the bubble interface. However a rough estimation of experimentally observed pressure pulse near the bubble is possible using the Bernoulli equation below

$$P(r,t) = P_\infty + \frac{R}{r}(P_V - P_\infty) + \frac{\rho}{2}\frac{R}{r}\dot{R}^2\left[1-\left(\frac{R}{r}\right)^2\right]. \qquad (4.20)$$

From the equation (4.20), it can be seen that as distance increases, pressure amplitude is decreased. We believe that pressure probe in the experiment of Nelson *et al.* was away from the bubble. If pressure probe is away from the bubble 10 times the minimum radius of the bubble, then pressure amplitude in the sensor will measure ~ O (10^{-1}) of the vapor pressure. Calculated pulse width of the pressure is ~30 μs, which is consistent with the one observed by the Inoue *et al*.

The histories of vapor temperature and interface temperature of the bubble are shown in Figure (4.7). It can be seen from the figure that during each collapse phase, vapor temperature rises to a very high value, but it remains below the melt temperature. Interface temperature also follows the similar trend during the collapse of the bubble *i.e.* the interface temperature rise. But it is expected that interface temperature should attain a value of saturated temperature corresponding to the vapor pressure under thermodynamic equilibrium. But what we observe in our calculations is that interface temperature is lower than the saturated temperature during the collapse phase. Possible reason could be due to use the simplified equation for the calculation of interface temperature.

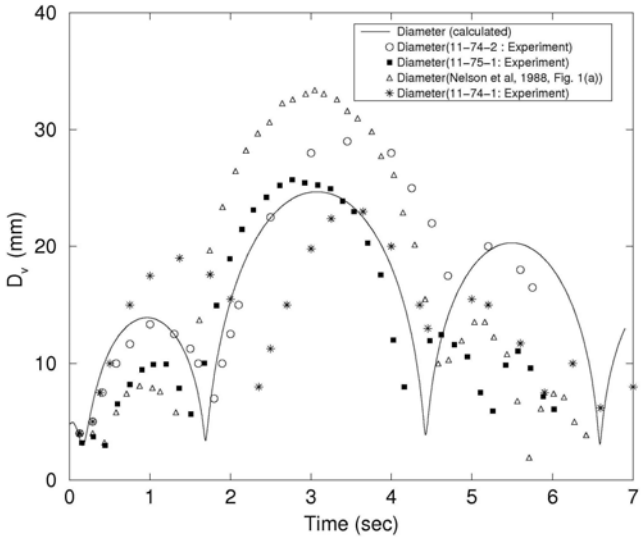

Figure 4.6: Time history of vapor pressure.

More rigorous analysis using full energy equation in the liquid side may be needed to estimate the interface temperature more accurately. So, further studies are needed to see the effect of interface temperature on the instability of the bubble dynamics. During the expansion phase of the bubble, vapor temperature fall below the interface temperature, which suggests that reverse heat transfer occurs *i.e.* heat flow into the bubble. Since the temperature difference is small, not much heat transfer occurs during this phase. Basically, vapor acts as a blanket around the melt, which is undesirable.

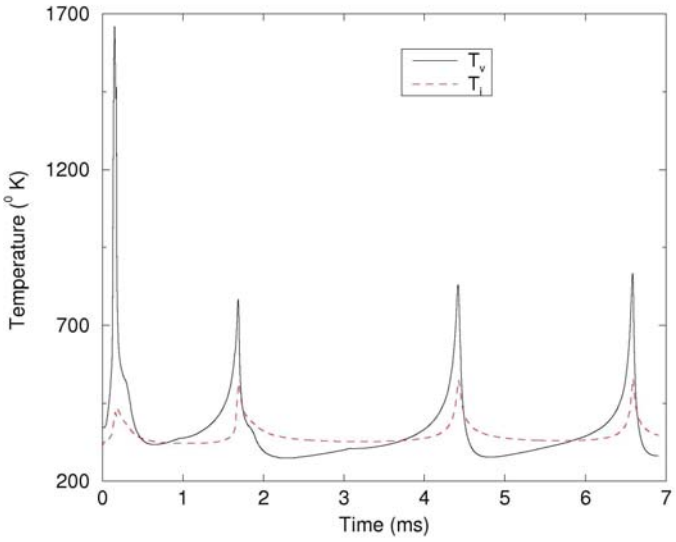

Figure 4.7: Time history of vapor temperature and interface temperature

4.6 SUMMARY

Present analysis gave a good qualitative agreement with the experimentally obtained bubble dynamics and the pressure pulse. Present results further suggest that for the same initial conditions different bubble dynamics are possible depending on the mode of

instability. This is due to many active modes, which are capable of triggering the explosion. This may be one of the reasons for the reported experimental results showing different bubble dynamics for the same initial conditions. Initial agreement of the present calculation with experimental data suggests that we may able to develop a tool, which can be useful for analyzing the melt fragmentation process in a single drop steam explosion with stability analysis. Present model can predict the fragmented mass during each successive collapse of the vapor bubble

5. MOLTEN POOL COOLABILITY: POMECO EXPERIMENTS

5.1 INTRODUCTION AND OBJECTIVES

5.2 POMECO FACILITY

The POMECO (POrous MEdia COolability) facility was designed for experimental studies on coolability of heat generating particulate debris beds. The test section was a stainless steel vessel with the cross section of 350×350 mm. Total height of the test section was 1400 mm, which included the upper vessel where water was supplied. Up to 370 mm high sand bed could be formed to simulate the debris. The test section contained an annular pipe of the same dimensions as the prototypic CRGT in a prototypic BWR (the TVO BWR). One CRGT and the debris mass associated as a unit cell was represented in POMECO. The decay heat for the scenario was chosen as that appropriate for 3-4 hours after the scram, i.e. about 1 MW/m^3. The maximum power available for the sand bed was 46 kW, which corresponds to the volumetric power of about 1 MW/m^3, for the POMECO vessel sand bed dimensions.

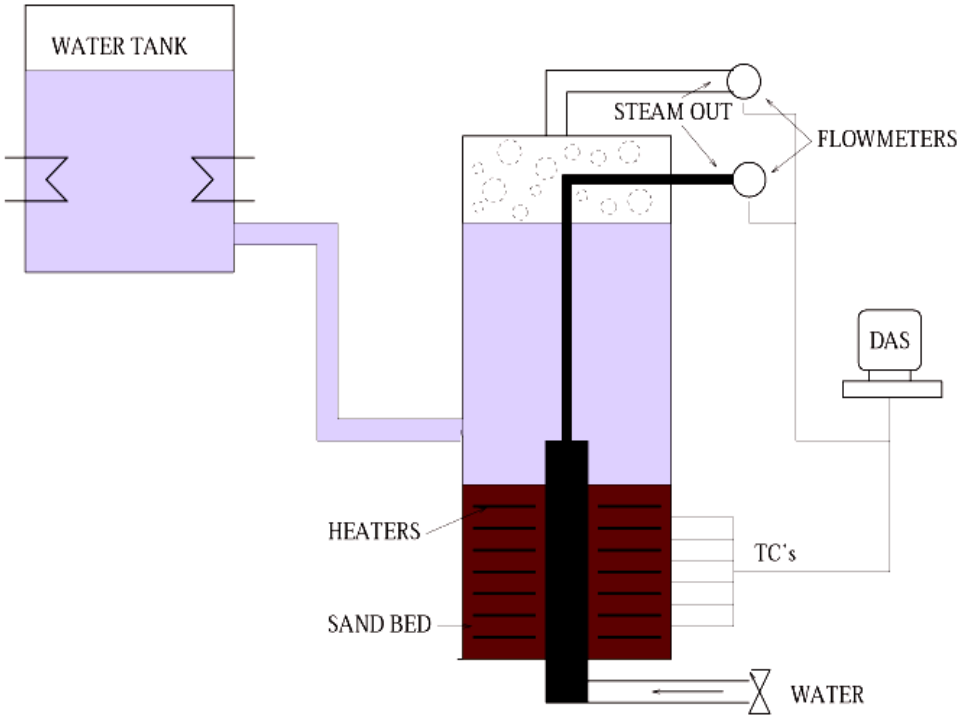

Figure 5.1: POMECO test facility.

The schematic of the POMECO (POrous MEdia COolability) facility, modified for this study to include the CRGT is shown in Figure 5.1. The POMECO facility consisted of water supply system, test section, heater power supply, instrumentation and the data acquisition (DAS) systems.

Some details of the test section are presentedin Figure 5.2. The height of the lower part is 500 mm and the height of the upper part is 900 mm. Figure 5.2 (b) also shows the configuration of the heaters and the thermocouples contained in the sand bed. Figure 5.2 (a) shows the axial cross section of the actual CRGT, which is employed in the sand bed contained in lower part of the POMECO facility.

The upper part of the CRGT annular pipe was closed with the cover, which contained holes. These holes were of the same flow area as the bypass inlet in the prototypic CRGT. The holes were designed to be open or closed. A pipe was connected to the cover of the CRGT annular pipe and it was led out of the POMECO facility, so that the steam generated in the annular pipe can be measured separately from that generated from the sand bed. The CRGT pipe was connected to a water line at the bottom, which could supply the same (or different) rate of water flow to the CRGT as in the prototypic BWR.

Thirty-three thermocouples were distributed at different locations in the particle bed as shown on the Figure 5.2 (b). To obtain the axial temperature variation and to determine the heat flux in the CRGT wall, 9 thermocouples were embedded at three different wall depths (Figure 5.2 a) and at three different axial positions along the CRGT height.

The dryout tests were started with fully saturated bed. The power input to the bed was increased in small steps until the dryout (i.e. the sudden increase in debris bed temperature) was recorded.

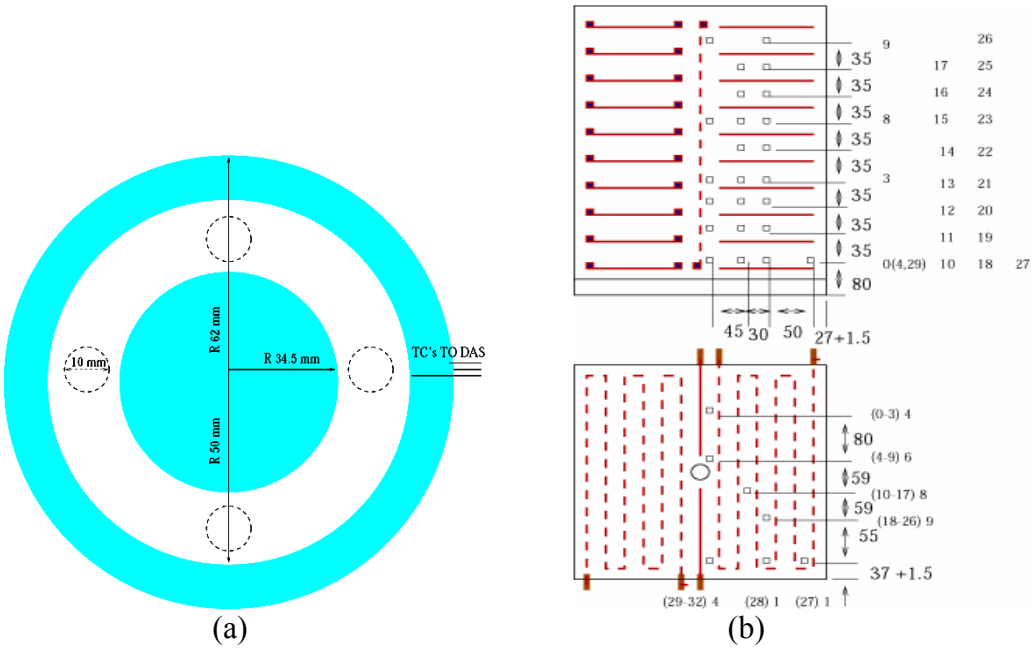

Figure 5.2: The CRGT design, heater and thermocouple distribution.

The quenching experiments were carried out by establishing a column of water above the dry particulate beds, which were initially heated up to 500ºC. All experiments were performed at atmospheric conditions.

5.3 RESULTS

5.3.1 POMECO experiments

POMECO experiments with three different particulate debris bed configurations were performed. The effects of porosity and presence of CRGT on the dryout heat flux and the quenching rate had been measured.

5.3.2 Dryout experiments

The following dryout experiments were performed within each test series on dryout heat flux:

- With no water flow in the CRGT pipe;
- Water supply flow from the bottom to the CRGT pipe;
- Water flow through the open the upper holes (bypass) in the CRGT pipe, no water addition from the bottom;
- Water flow through the open upper annular part of CRGT, no water addition from the bottom.

In the first two test series (experiment with only top flooding) no dryout at the full power density of 0.98 MW/m^3 was observed (Table 5.1 and Table 5.2).

In the tests DRC-1 this result is confirmed by the Lipinski model, which shows that for such bed configuration dryout can be expected at the power supply of about three times larger than that provided by the POMECO test section. Experiments with subcooled and saturated water in the CRGT showed similar results.

In the previous POMECO experiments (test series homo-2 described in Konovalikhin, et al., 2000) for the bed of the same configuration as in the test DRC-2 the measured dryout heat flux was 222 KW/m^2. This result is in good agreement with the prediction by Lipinski model (see Table 5.1). But during the DRC-2.1 experiment with the CRGT inside the bed no dryout was obtained (Table 5.2). This can be explained by the additional coolability capacity of the bed, provided by the CRGT. The heat removal rate through the CRGT was estimated as 15 kW, which, added to the Lipinski model value, could provide the estimation of 350 kW/m^2 as the dryout heat flux for such test conditions.

Table 5.1. Experimental conditions and results for the sand bed with porosity 0.4 and mean particle size 1.9 mm.

Test	Water flow rate in the CRGT, kg/s	Experimental dryout heat flux, kW/m^2	Dryout heat flux Lipinski model, kW/m^2	
			Without CRGT	With CRGT
DRC-1.1	-	>327	932	1061
DRC-1.2	0.0625 (10°C water)	>327	932	1077
DRC-1.3	0.0625 (85°C water)	>327	932	1094

Table 5.2. Experimental conditions and results for the sand bed with porosity 0.36 and mean particle size 1.0 mm

Test	Water flow rate in the CRGT, kg/s	Dryout heat flux, kW/m^2	Dryout heat flux Lipinski model, kW/m^2	
			Without CRGT	With CRGT
DRC-2.1	-	>327	226	350

In the third test series the bed with the similar mean particle size as in the previous DRC tests and low porosity of 0.26 was examined. The first experiment, DRC-3.1, showed (Table 3) that the presence of the CRGT increases the dryout heat flux significantly.

Earlier series of POMECO experiments conducted with similar particle bed composition had shown a good agreement between the experimental result and prediction by Lipinski model (Konovalikhin, et al., 2000).

From the comparison of these two experiments the additional cooling capacity provided by CRGT can be estimated as 10 kW for this bed configuration. It can be seen that addition of this value to the Lipinski model prediction gives a result, which is very close to the experimental.

Table 3. Experimental conditions and results for the sand bed with porosity 0.26 and mean particle size 0.8 mm.

Test	Water flow rate in the CRGT, kg/s	Dryout heat flux, kW/m^2	Dryout heat flux Lipinski model, kW/m^2	
			Without CRGT	With CRGT
DRC-3.1	-	133	51	132
DRC-3.2	0.0625 (85°C water)	154	51	154
DRC3.3	0.00625	166	51	170
DRC-3.4	Open upper holes	275	-	-
DRC-3.5	Open top part (cross section)	251	-	-

The tests DRC-3.2 and DRC-3.3 were conducted in order to investigate the enhancement of the dryout heat flux by the water flow in the CRGT. Two different flow rates were used: 0.0625 kg/s (prototypic) and 0.00625 kg/s of 85ºC water. As it can be seen in the Table 3, water flow enhances the dryout heat flux. In the test DRC-3.2 with flow rate of 0.0625 kg/s the additional heat removal is provided due to the heating of flowing water without vaporization. From the experimental data the heat flux to the water inside the CRGT estimated as 40 - 50 kW/m^2.

The comparison between experimental result of the test DRC-3.2 and Lipinski model gives good agreement (with consideration of heat removal through the CRGT wall to the water overlayer and heating of water inside CRGT). In the test DRC-3.3 partial vaporization of coolant was registered, which explains higher dryout heat flux in

comparison to that in the two previous experiments. To analyze this experiment by the Lipinski model steam generation rate in the CRGT was calculated employing the methodology described in (Konovalikhin, et al., 2000). The results of the comparisons are presented in the Table 3.

The objective of the test DRC-3.4 was to investigate dryout behavior in the situation, when saturated water can be delivered into CRGT pipe through the bypass flow openings in a BWR. For this purpose four holes, with total flow area equal to that in the BWR's bypass, were kept open during this test. As a result (see Table 3) a great enhancement in dryout heat flux was obtained. The improvement can be caused by intensive boiling inside the CRGT line, which resulted in significantly higher total steam discharge flow rate in comparison to those in the previous tests.

The test DRC-3.5 simulated the situation when the upper part of CRGT pipe is melted down and water could penetrate into the tube from the layer above. The total steam discharge was slightly lower in comparison to that in the test DRC-3.4, and, correspondingly, the experimental dryout heat flux was less (see Table 3).

It can be explained by the fact that during the test DRC-3.4 the steam release rates were recorded at the outlets of the CRGT pipe and water tank, but in the test DRC-3.5 only water tank steam discharge flow rate was measured, because the upper part of CRGT pipe was removed, and part of the steam discharged from the CRGT could be directly condensed during the passage through the water overlayer.

5.3.3 Dry bed cooling by water flow in CRGT

The experiment DRYFL was performed in order to obtain the heat removal rate from the dry bed by the water flow in the CRGT pipe without top flooding. The objective of this test was to measure heat extraction by water in the CRGT during cooling down of the bed from 450°C to 100°C.

Table 5.4. Experimental results of cooling test for homogeneous particle bed (porosity – 0.4, mean particle size – 1.9 mm); power supply – 4200 W; coolant t=85°C.

Test	Initial bed temperature, °C	Water flow rate in the CRGT, kg/s	Average steam discharge flow rate, kg/s	Quenching time, s
DRYFL	450	0.0625 (85°C water)	0.007	450

Experimental conditions and results of the test are presented in the Table 5.4. This test can be characterized by a relatively high CRGT heat removal rate, due to a partial vaporization of water (85ºC at inlet) during the passage through the CRGT pipe.

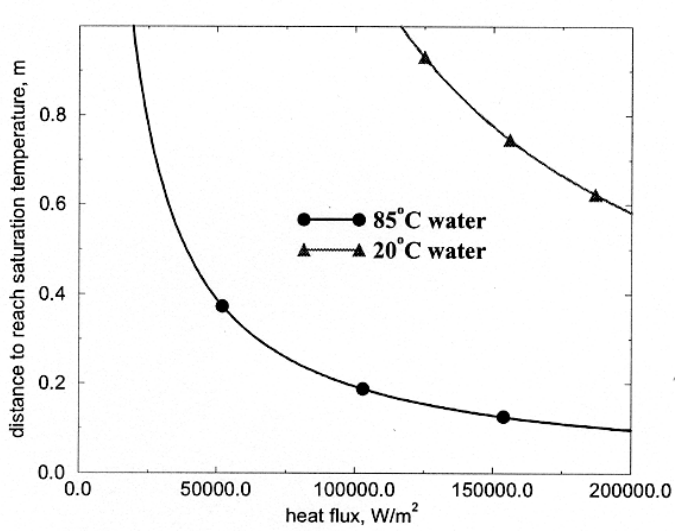

Figure 5.3: Calculated water saturation distances

The heat flux was estimated to be 150 kW/m^2. As it can be seen in Figure 5.3, calculations for the water saturation distance with experimental conditions presented above show that subcooled water cannot reach the saturation temperature. In other words, the dry bed with constant power supply of 4.2 kW and flow rate in CRGT of 62.5 kg/s of 20ºC water would not be coolable.

5.3.4 Quenching experiments

Three series of experiments with different particle bed configurations to study the effects of porosity and the presence of CRGT on the quenching process of the dry bed have been carried out. Tables 16-18 list the experimental results on quenching rates for the homogeneous particle beds with different experimental conditions. From the temperature histories at various locations in the particulate layer, the quenching time was determined by a rapid drop in the particle temperature (down to about the saturation temperature of water at the system pressure).

Table 5.5. Experimental results of quenching tests for homogeneous particle bed (porosity – 0.4, mean particle size – 1.9 mm); power supply – 4200 W; coolant temperature – 85ºC.

Test	Initial bed temperature, °C	Water flow rate in the CRGT, kg/s	Average steam discharge flow rate, kg/s	Quenching time, s
QC-1.1	500	-	0.014	240
QC-1.2	500	0.0625 (85°C water)	0.02	175

The water flow through the CRGT decreased the quenching times (Table 5.5 and Table 5.6) due to the additional heat removed by the flowing coolant. During the tests QC-2.2 and QC-2.3 two different coolant flow rates are compared: 0.0625 kg/s (prototypic) and 0.00625 kg/s. During the test QC-2.3 with lower water flow more intensive water vaporization was registered, which caused the decrease in quenching time compared to the test QC-2.2.

Table 5.6. Experimental results of quenching tests for homogeneous particle bed (porosity – 0.36, mean particle size – 1.0 mm), power supply – 4200 W; coolant temperature – 85 ºC.

Test	Initial bed temperature, °C	Water flow rate in the CRGT, kg/s	Average steam discharge flow rate, kg/s	Quenching time, s
QC-2.1	450	-	0.009	210
QC-2.2	450	0.0625 (85°C water)	0.011	160
QC-2.3	450	0.00625 (85°C water)	0.013	140

Two main observations can be drawn from experimental results of QC-3 test series:

- the decrease in bed porosity resulted in a significant increase of quenching time;
- the presence of CRGT in the bed intensifies the quenching process.

In the tests QC-2 and QC-3 (see Table 5.6 and Table 5.7) the mean particle sizes were quite similar, but porosity value in the test series QC-3 was lower. It led to the slower water penetration through the bed due to a higher capillarity and lower steam generation rates (Table 5.7).

The test QC-3.4 was performed with open upper holes, which simulate the bypass openings in a BWR CRGT. Through these holes saturated water from the water overlayer could access the CRGT from above and provide intensive boiling and steam release inside the pipe.

Table 5.7. Experimental results of quenching tests for homogeneous particle bed (porosity – 0.26, mean particle size – 0.8 mm), power supply – 4200 W; coolant temperature – 85 ºC.

Test	Initial bed temperature, °C	Water flow rate in the CRGT, kg/s	Average steam discharge flow rate, kg/s	Quenching time, s
QC-3.1	450	-	0.003	1300
Qc-3.2	450	0.0625 (85°C water)	0.0035	1200
QC-3.3	450	0.00625 (85°C water)	0.004	1100
QC-3.4	~470	Open upper holes	0.007	1000
QC-3.5	450	Open upper cross section	0.005	950

The test QC-3.4 did not lead to a significant decrease in the quenching time because the initial bed temperature was higher in comparison to that in previous tests of the series QC-3. The last quenching experiment QC-3.5 with the open annular cross-section represented the situation with melted down upper part of CRGT. The test showed that the larger flow area provided more intensive water penetration into the CRGT, thus,

providing more intensive heat transfer, which led to a decrease in the quenching time (Table 5.7) in comparison to that in the previous experiments of the test series QC-3.

5.4 ANALYSIS

5.4.1 POMECO experiments

A simple zero-dimensional integral analysis has been performed based on consideration of hydrodynamic flooding due to the steam formation. The basic assumptions were that the water penetrates the debris bed at a constant velocity, which is uniform across the bed, and the steam is generated immediately after the contact of water with the solid particles. In addition, it was assumed that the hot particles are completely quenched and cooled to water saturation temperature as the water penetrates through the debris bed. The quenching rate of the bed is directly proportional to the penetration rate. The following relation for the quenching time can be written:

$$\Delta t = \frac{\rho_{sol} C_{p,sol} (1-\varepsilon) V (T_{sol} - T_{sat})}{(G_w H_{fg} + W_{CRGT}) - W} \qquad (5.1)$$

Here, heat removal rate through CRGT W_{CRGT} consists of heat removed through CRGT structure (wall) to the water overlayer, heat to heat up the coolant inside the CRGT ($G_{w,CRGT}\Delta T$) and the latent heat of vaporization ($G_{w,CRGT}H_{fg}$). The numerator in this ratio is responsible for the total heat, which has to be removed in order to quench the bed and the lower term is the cooling down (quench) rate.

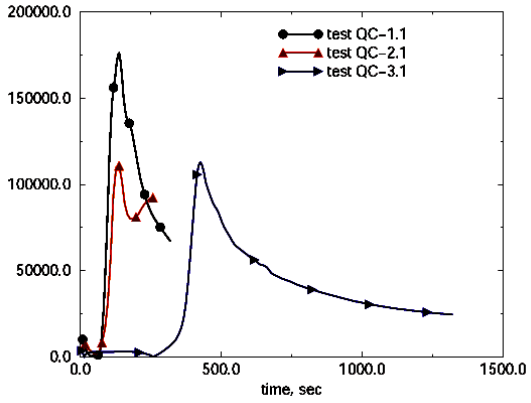

Figure 5.4: Inversely predicted surface heat flux in quenching experiments QC-1.1, QC-2.1 and QC-3.1

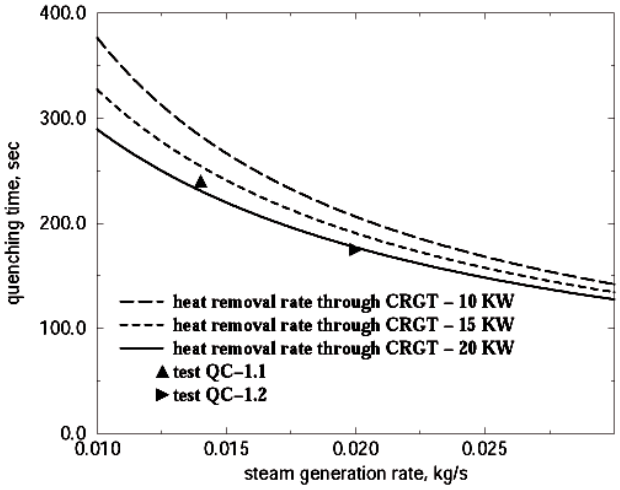

Figure 5.5: Comparison between experimental and calculated results of QC-1 test series.

The CONTA code was employed to estimate heat removal rate through the CRGT structure. The results of the calculations are presented in Figures 5.4 and 5.5. For the given experimental conditions the heat fluxes in the CRGT wall are between 100 KW/m^2 and 170 KW/m^2. Higher heat flux in the QC-1.1 test is due to the higher initial bed temperature.

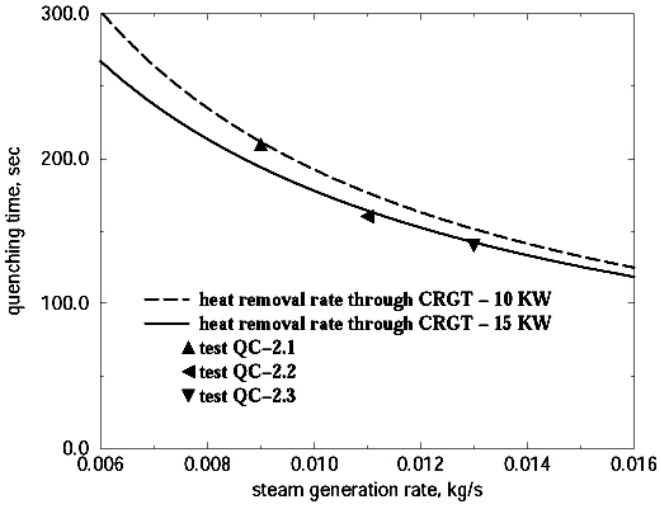

Figure 5.6: Comparison between experimental and calculated results of QC-2 test series.

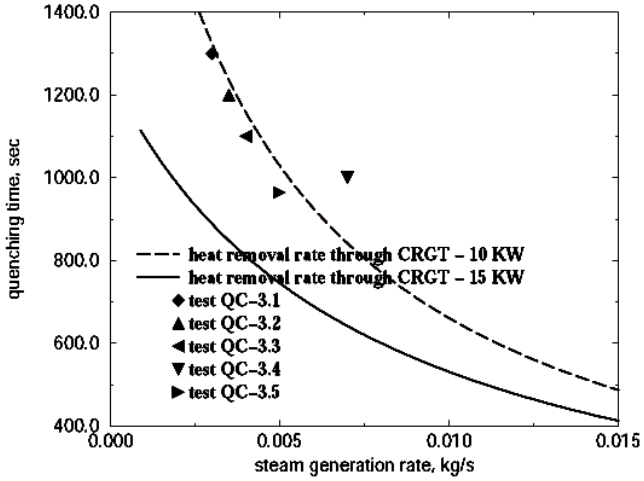

Figure 5.7: Comparison between experimental and calculated results of QC-3 test series.

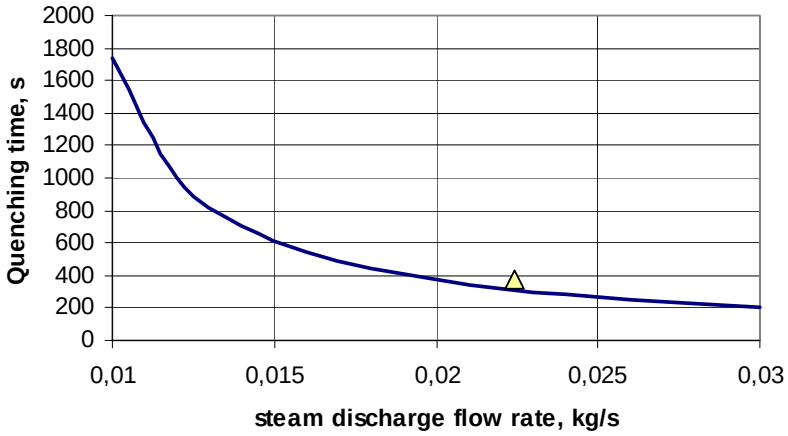

Figure 5.8: Comparison between experimental and calculated results for the HT-1.

Using the method described in (Konovalikhin, et al., 2000) and values predicted by the CONTA calculations all the quenching experiments performed in the POMECO test series were analyzed. The results of the analysis are depicted in Figure 5.6, 5.7 and 5.8. As it can be seen from these Figures the experimental results of the first test series agree best with the calculations with average heat removal rate through CRGT structure taken as 20 kW; for the second test series - between 10 and 15 kW and for the last test series - 10 kW.

The Eq. (5.1) was applied to predict the quenching time for the high temperature debris bed test (Experiment HT-1, carried out at COMECO facility for the particle bed of porosity 0.4 and mean particle size 2 mm). The model proved to be as well valid for the higher temperature of the debris bed region.

5.5 SUMMARY

The POMECO experiments had shown that the presence of the control rod guide tubes offers a significant additional cooling capacity for the particulate debris bed, which leads to enhancement of the dryout heat flux and the quenching rate. Heat removal rate through CRGT structure was found to be 10-15 kW depending on the surrounding porous media and temperature regime. Water flow rates in the CRGT result in additional enhancement of the dryout heat flux and intensification of quenching process.

Lipinski model with addition of CRGT coolability potential was employed to analyze the POMECO dryout experiments. Reasonable agreement between the experimental and calculated results was obtained.

Characteristic times for quenching were computed by the model, which combines parameters of the process (V, p_{over}, T_{sol}, T_w, W), geometry (A_{bed}, d_{dwnc}) and physical properties (H_{fg}, $C_{p,w}$, ρ_w, μ_w, $C_{p,sol}$, ρ_{sol}, ε). Good agreement between experimental and calculated results has been achieved for the POMECO experiments and the high temperature debris bed experiment at the COMECO facility.

6. MOLTEN POOL COOLABILITY: COMECO EXPERIMENTS

6.1 INTRODUCTION AND OBJECTIVES

The objective of the COMECO experimental program within the scope of the APRI-5 project is to perform experimental investigations on the simulant corium material coolability and to assess the enhancement of the coolability employing downcomers in the melt pool. As well, the analytical investigation of the experimental data of current and previous COMECO experiments, which would allow assessing the existing models on crust growth, melt pool quenching time, water ingression, etc.

A series of experiments with the downcomers are planned to be performed, covering a number of test conditions.

6.2 EXPERIMENTS

6.2.1 The COMECO facility

The COMECO facility (Figure 6.1) consists of a test section (200 × 200 mm cross section), with the maximum melt pool height of 300 mm. The test section walls are made of 25 mm thick carbon steel. The test section is connected to the upper tank (1000 mm high). Water is supplied to the upper tank via the water line from the heated water storage. The melt pool is heated directly by heaters, located outside the test section on the four sidewalls. The four heaters can deliver the maximum power of 16 kW to the melt pool, i.e., the maximum power density in the melt pool of 1.33 MW/m^3 could be attained.

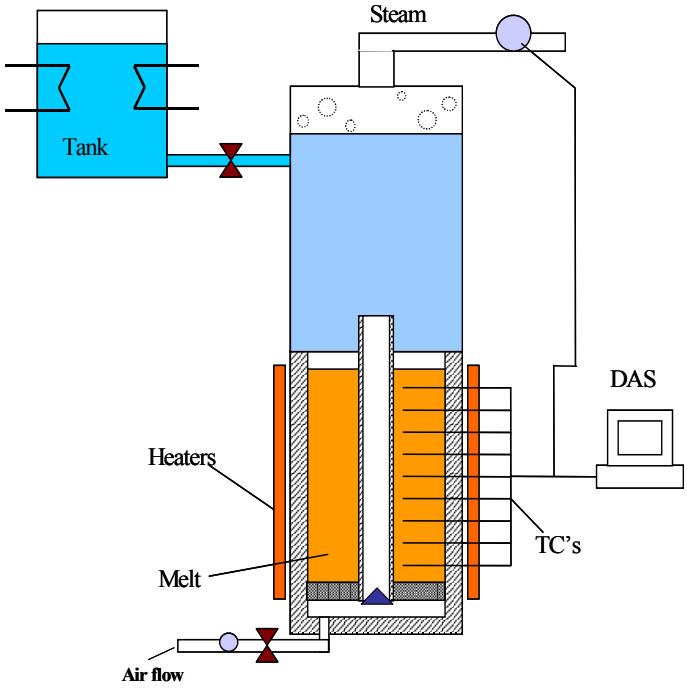

Figure 6.1: The COMECO test facility.

A downcomer (with the outside diameter d_o=50 mm and the inside diameter of d_i=45 mm) is placed in the center of the test section. The air supply system is installed at the bottom of the test section to simulate the con-condensable gas release. Flowmeters were installed on the steam outlet lines from the CRGT and the upper tank and also on the water supply line, to measure the water flowrate through the CRGT.

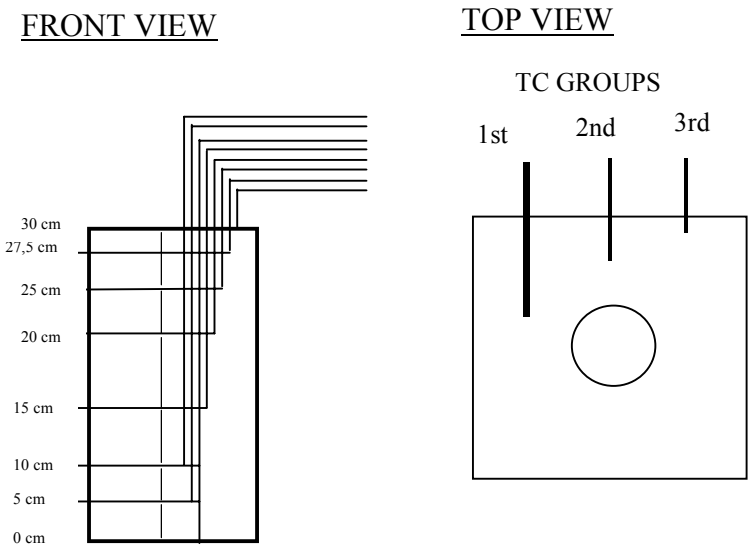

Figure 6.2: Thermocouple distribution in the COMECO facility.

The temperature readings were obtained from 24 thermocouples, distributed uniformly within the melt pool. The thermocouples are placed at 8 axial elevations and at 3 radial locations within the melt pool. The distribution of the thermocouples in the COMECO facility is shown on the Figure 6.2.

Before the experiment, the binary oxide mixture was heated up to the initial temperature of about 1300°C in an induction furnace. The test section was also heated up to about 1100°C in order to avoid the thermal shock and deformation of the test section when the melt was poured into the test section from the induction furnace. Afterwards, the requisite air flow rate is established through the test section and the melt is poured into the test section.

Series of quenching experiments are performed. The experiments should provide a database for the melt pool coolability with the presence of downcomer in the melt pool. The experiments to be performed:

- Experiments with a closed downcomer and without external heating. These experiments would define a reference case for the water ingression and cooling down rates in the non-heated melt pool.

- Experiments with a closed downcomer and with external heating. These experiments would define a reference case for the water ingression and cooling down rates in the heated melt pool.

- Experiments with open downcomer and with/without external heating. The experiments would investigate the coolability enhancement of the melt pool, offered by the use of a downcomer.

6.2.2 Experimental results and preliminary findings

Three experiments in the COMECO facility with downcomers were performed:

- Experiment D-1 with a closed downcomer and without external heating.

- Experiment D-2 with a closed downcomer and with external heating (total heaters power was 16 kW, which corresponds to 1.3 MW/m^3. COMECO test section failed (the melt leaked) during this experiment. The experiment has to be repeated in the near future.

- Experiment T-1 with an open downcomer and with external heating.

Prior to all tests the additional air was injected from the bottom of the test section (at a flow rate of about 50 l/min, which corresponds to the interfacial velocity of about 2 cm/sec).

Preliminary findings of the new experiments:

- With the airflow rate, which corresponds to the interfacial velocity of about 2 cm/sec (prototypic conditions) a big amount of additional water was entrapped with the passing airflow and removed from the upper tank of the test section.

- Additional system, which condenses and removes the entrapped water, had to be constructed, to provide a possibility to measure the amount of the water, entrapped during the experiments. The system was constructed for the test T-1.

- The presence of the downcomer reduced the quenching times.

- The additional bottom cooling of the melt pool, provided via the supply of water to the bottom of the melt pool through the downcomer was not as efficient as expected.

6.3 ANALYSIS

Extensive analysis of the previous COMECO experiments (with the control rod guide tube model in the COMECO test section) was carried out. The aim of the work was to assess available models for the prediction of the COMECO experimental results.

6.3.1 Prediction of the quenching time

A zero-dimensional integral analysis has been performed based on consideration of a balance between the heat release and the heat removal from the melt pool. The following relation for the cooling time was written:

$$\Delta t = \frac{(\rho_m V_m (C_{p,m} \Delta T_m + H_{fus,m})) \frac{\delta}{H}}{(q_{CRGT} \pi d_{CRGT} \delta + q_{out} S) - W} \qquad (6.1)$$

As only partial quenching of the melt pool was reached during the experiment, the equation above was applied to estimate the partial quenching times for the experiment CT-1 and the first four phases of the experiment CT-3. The calculation results are presented in the Table 6.1.

Table 6.1. Comparison of experimental and calculated quenching times.

Experiment	Experimental water ingression depth, cm	Experimental partial quench time, sec	Calculated quench time, sec	Calculated quench time with no CRGT, sec
CT-1, Phase 3	2.5	105	114	120
CT-3, Phase 1	2.5 5.0 10.0	99 258 438	106 235 436	122 259 597
CT-3, Phase 2	2.5 5.0 10.0	54 138 194	51 116 254	54 135 366
CT-3, Phase 3	2.5 5.0 10.0	64 101 159	77 100 216	80 110 268
CT-3, Phase 4 and Phase 5	2.5 5.0 10.0 15.0	67 99 182 251	88 171 181 251	96 190 248 426

Calculated quenching time with no CRGT was estimated without taking into account the additional heat flux on the CRGT wall. In this case (Table 6.1) the predicted quenching times become longer, compared to the measured values. The difference between the quenching time increases with the growth rate of the crust layer.

As it is seen from the Table 6.1, a reasonable prediction of the quenching times was obtained for all the phases of the experiments. For the later phases of the experiment CT-3, the calculations predict later occurrence of the quenching compared to the recorded experimental results. The reason for this are the lower temperatures in the upper part of the melt pool during the later phases of the experiment, as the melt pool was reheated after each phase. During the later phases it was not possible to achieve the homogeneous temperature distribution when reheating the melt within the pool, therefore the temperatures in the upper part of the pool remained below the melt freezing temperatures even after the reheat, i.e. the flow paths for the water to penetrate into the crust were already formed during the earlier phases and the coolant was penetrating the crust at higher rates, compared to the calculated values.

6.3.2 Bulk cooling

Bulk cooling establishes soon after the coolant layer is established on the top of the melt pool. The bulk cooling is a short-term phenomenon, which is terminated by the formation of a stable interfacial crust on the top of the melt pool. The bulk cooling results in high heat fluxes (up to 4 MW/m^2) as a consequence of conduction/radiation across area enhanced melt/coolant interface.

During the early phases of the coolability process the surface temperature of the melt pool is above that required for film boiling of water so that a vapor film separates the melt surface from the water.

This initial phase of the melt pool-water interactions could be investigated applying the classical Berenson equation for zero-gas flux film boiling:

$$q_{out} = \frac{k(T_m - T_{sat})}{\delta_{Ber}} + h_{rad}(T_m - T_{sat}) \qquad (6.2)$$

This equation was applied while assessing the maximum heat flux during the bulk cooling (Experiment CT-1 Phase 3). As it is seen from the Figure 6.2, the calculated maximum heat removal value for the bulk cooling was about 120 kW, which corresponds to q"=3.156 MW/m^2. The bulk cooling heat transfer rate decreased rapidly due to the reduction of the temperature in the upper layer of the melt pool and the onset of the crust formation on the top of the melt pool.

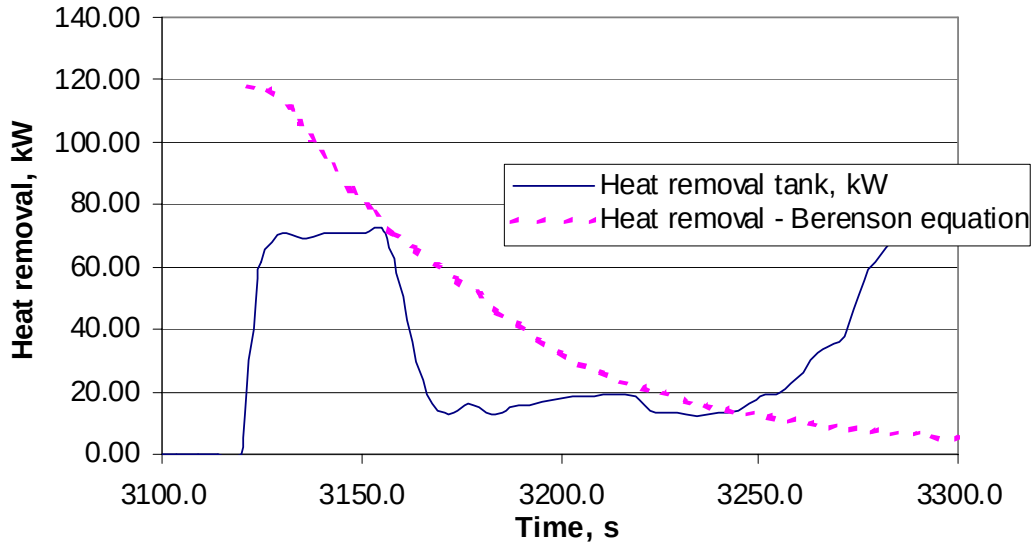

Figure 6.3: Comparison of experimental data and predicted values for the bulk cooling phase.

The results for the maximum value of the bulk cooling heat transfer are also supported by the experimental results of the experiment CT-3, where the higher capacity flow meter was installed. The maximum value for the bulk cooling heat transfer was close to 150 kW for the experiment CT-3, Phase V, corresponding to q"=3.945 MW/m^2.

6.3.3 Crust growth

For the prediction of the crust growth rate the model developed by Farmer was modified and used for the analysis of COMECO experiments.

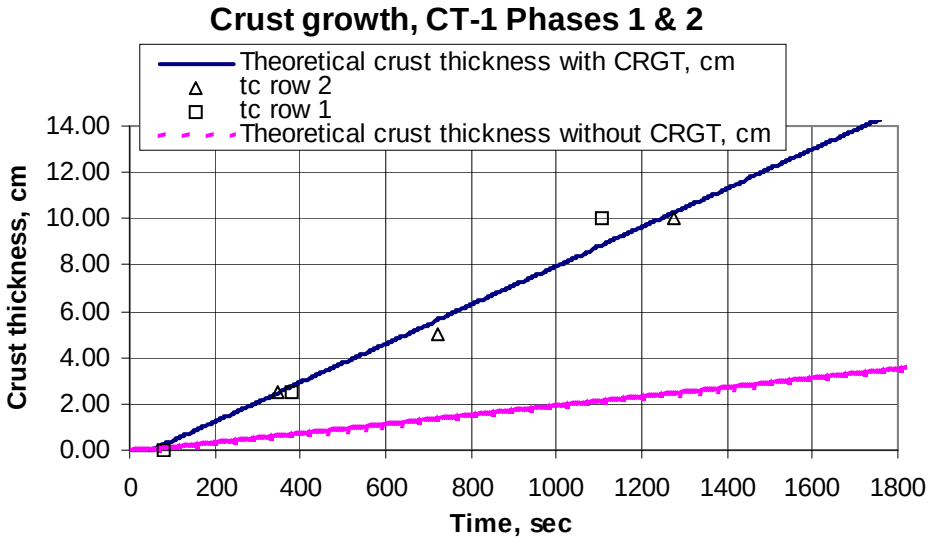

Figure 6.4: Crust growth during Phases I and II of the experiment CT-1.

For the COMECO experiments the model can be reformulated as:

$$\rho_c \Delta e_{ls} \frac{d\delta}{dt} = k_c \frac{(T_f - T_I)}{\delta} - \frac{q_c}{2} + q_{CRGT} \qquad (6.3)$$

The results of the average crust growth rate, for the Phases I and II of the experiment CT-1 are presented on the Figure 6.4. During the first two phases of the experiment there was no water layer above the melt pool and, therefore, the melt was cooled under the dry cavity conditions.

As it is seen from the Figure 6.4, the experimental data (thermocouples in the rows 1 and 2) are in good agreement with the predictions of the Farmer model for the crust growth in the dry conditions. The crust growth rate for the conditions when the CRGT is not present is also plotted on the Figure 6.4. In this case the crust growth rate for the dry cavity would be significantly lower. The crust thickness of 10 cm for the case with no CRGT would be reached only at t=5088 sec, according the present model (vs. about 1200 sec when having a flow inside the CRGT).

6.3.4 Water ingression

Farmer's model for water ingression

For the case, when the crust is treated as permeable, the onset of the water ingression occurs when the total heat flux from the crust falls below the corresponding dryout heat flux for the upper surface of the melt pool:

$$\rho_c \Delta e_{sat} \frac{d\delta}{dt} = q''_{d,c} - q_c + q_{CRGT} \qquad (6.4)$$

The particle bed was established above the melt pool during the Phase III of the experiment CT-3. As it was shown during the earlier experimental series on the dryout heat flux in particle beds carried out in POMECO facility, the Lipinski correlation (Lipinski, 1984) predicts well the effective dryout limit.

Considering the dryout heat flux of 220000 W/m^2, the experimental data were plotted against the Farmer's model predictions. In Figure 6.4, the water on the top of the melt pool was supplied at t=3200 sec and the upper 10 cm of the melt pool were quenched in 600-700 sec. As it can be noted the Farmer's model provides a good prediction for the crust growth rate for the solidification time of the lower portions of the melt pool (15 cm deep), when using the Lipinski model calculated value for the dryout heat flux in the particle bed equal to 220000 W/m^2. For the upper portion of the melt pool, the solidification during the experiment CT-1, Phase 3 occurred much faster when compared to the Farmer's model. The correct prediction for the solidification time can be obtained when applying higher values for the dryout heat flux (constant in time), equal to 0.6 MW/m^2 (Figure 6.6).

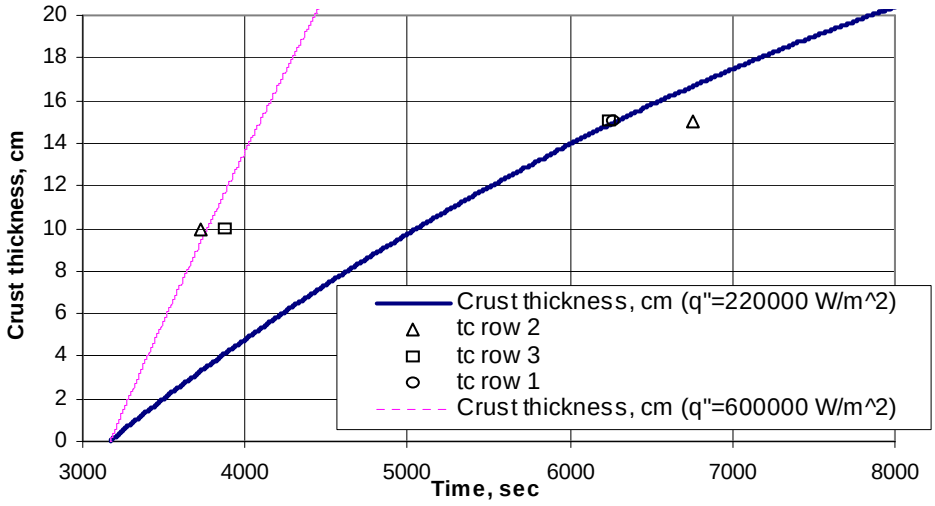

Figure 6.5: Comparison of CT-1 Phase III experiment data and crust growth rate, calculated using Farmer's model.

This can be explained as follows: when the quenching process started at the beginning of the Phase III, there was no particle bed on the top of the melt pool. Therefore, during the initial stages of the process the dryout heat flux was much higher, compared to the Lipinski model estimation. During the quenching process the particle bed was formed and, subsequently the dryout heat flux was reducing, therefore reducing the overall crust growth rate.

Since only average values of the dryout heat flux, independent of the debris accumulation with time, were used in the assessment of the crust thickness presented in Figure 6.6, additional analysis on the dryout heat flux behavior during the experiment was carried out.

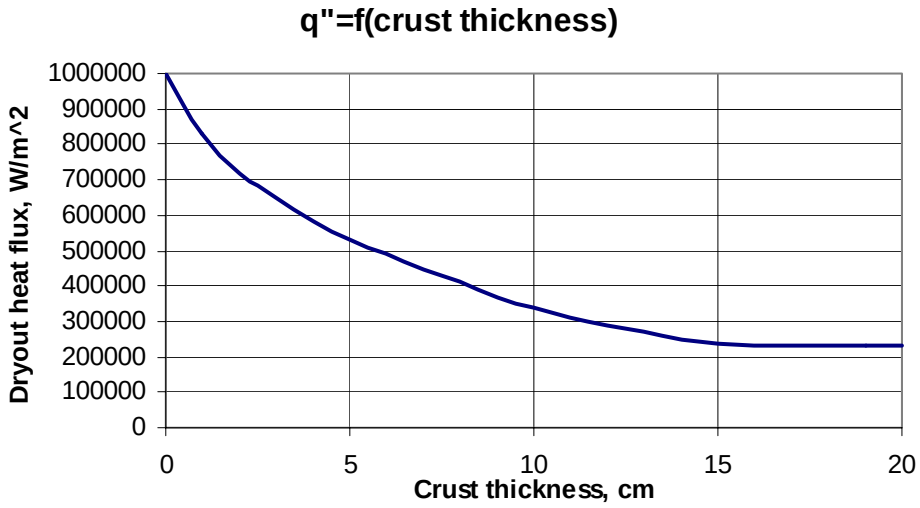

Figure 6.6: Assumed dryout heat flux during CT-1 Phase III.

As no information on the exact time-dependent values of this parameter are available from the experimental data, the dryout heat flux was assumed to be equal to the dryout heat flux for a flat plate (i.e. close to 1 MW/m^2) at the beginning of the test CT-1, Phase III (Figure 6.7). The dryout heat flux was decreasing during the test, as the crust thickness increased.

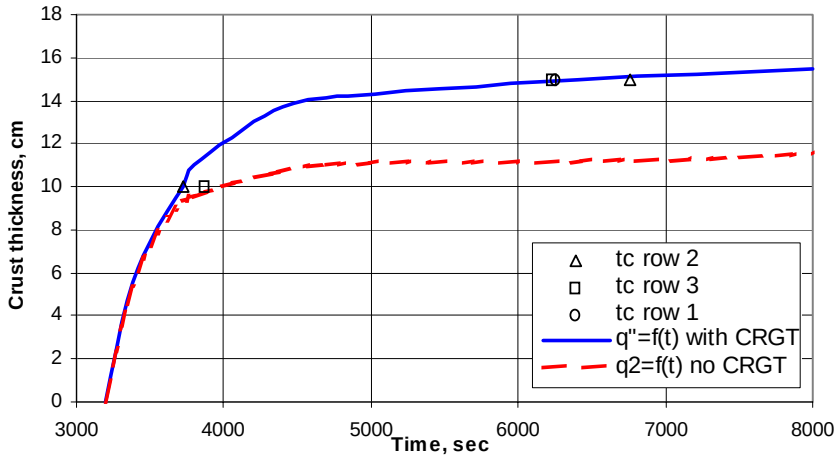

Figure 6.7: Calculated crust thickness during CT-1 Phase III.

Assuming the dryout heat flux, shown on the Figure 6.6, the crust growth rates were recalculated for the test CT-1, Phase III. In this case, a variable dryout heat flux q"$_{d,c}$ was used. Two cases were calculated: with and without the CRGT. The results of the calculations are plotted in the Figure 6.

As it is seen from the Figure 6.7, at the beginning of the quenching process there is no significant difference between the crust growth rates for configurations with/without the CRGT in the melt pool. At the beginning of the process the dryout heat flux was much

greater than the heat removal rate through the CRGT. During the later stages of the process, however, the dryout heat flux reduced significantly due to the formation of the particle bed on the top of the melt pool, thereby limiting the total heat removal rate from the melt pool. In these later stages the additional heat removal through the CRGT provides a significant contribution to the overall crust growth (Figure 6.7).

6.4 CONCLUSIONS

A series of experiments at the COMECO facility with the presence of a downcommer in the melt pool are being performed. The preliminary experimental findings indicate, that the presence of the downcommer reduces the melt pool layer quenching times. However, the effect of the downcommer is not as great as expected and as indicated by the previous series of POMECO experiments for the particulate debris bed coolability. The experimental program will continue and the obtained results will be presented and analyzed.

The analysis of previous set of COMECO experiments (with a control rod guide tube model in the test section) was carried out. The melt pool quenching times, crust growth and water ingression rates were analyzed.

The analysis of the experimental results was carried out for various phases of the quenching process. The zero-dimensional model derived from the heat balance of the test section provides a good prediction for the quenching times, recorded during the COMECO experiments. It shows that the efficiency of the heat removal capacity offered by the CRGT's increases with the crust thickness. The bulk cooling resulted in high heat fluxes during the first moments of the experiments. The Farmer's model for the crust growth and water ingression provided good estimations of the measured processes.

The COMECO experimental program will continue and the experimental database for the melt pool coolability with the presence of a downcommer will be compiled. Also, the analytical work in the melt coolability – related areas will be pursued.

7. MOLTEN POOL CONVECTION: SIMECO EXPERIMENTS

7.1 INTRODUCTION AND OBJECTIVES

Experiments are carried out in SIMECO (SImulation of MElt Coolability) test facility to study natural convection heat transfer and mixing phenomena in a molten pool. SIMECO test facility represents a slice of the hemispherical lower head of the vessel. The experimental study determines the thermal load imposed on the boundaries of an internally heated spherical stratified pool. This study is important for the assessment of the reactor pressure vessel integrity and for the accident management scheme of in-vessel melt retention by cooling the lower head from outside. Previously, one- and two-layers experiments were performed in a SIMECO facility. Effects of different internal heat generations and of the density differences between the layers are to be investigated.

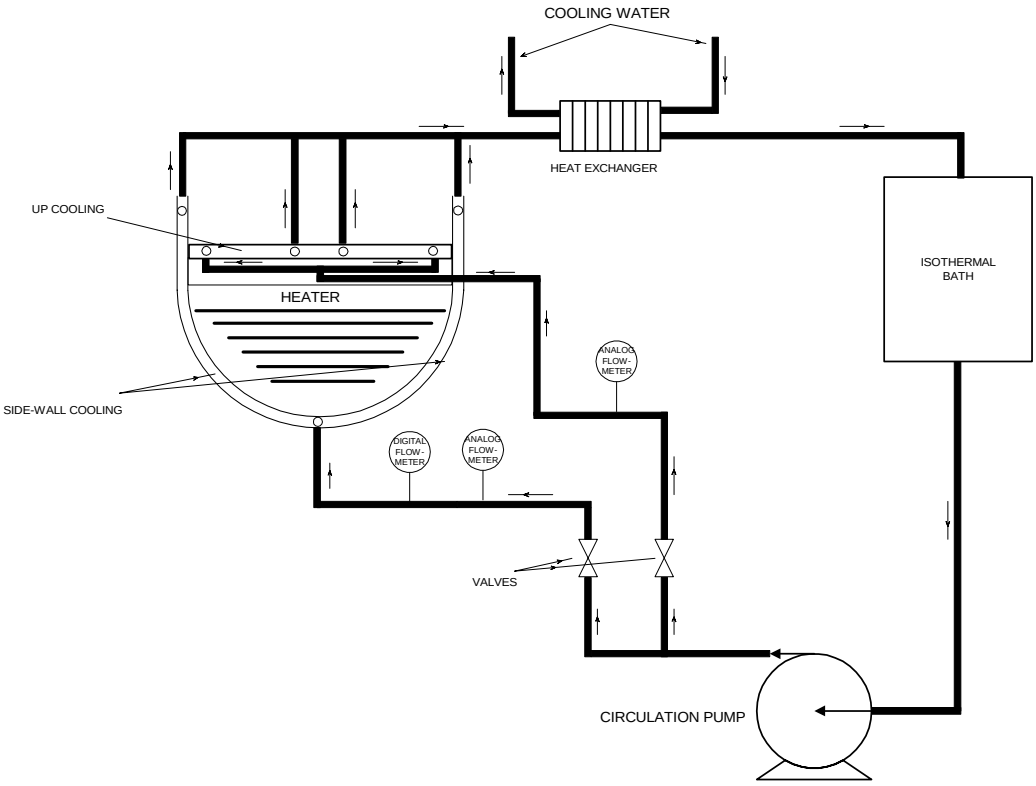

Figure 7.1: The SIMECO experimental facility.

7.2 THE SIMECO FACILITY

The SIMECO experimental facility as shown in Figure 7.1 consists of a slice type vessel, which includes a semi-circular section and a vertical section, representing the lower head of the reactor vessel. The size of the facility is scaled to be 1/8 of prototype PWR type reactors. The vessel's sidewall is represented by a thick brass plate, which is externally cooled by a regulated water loop. On the top of the vessel a heat exchanger with regulated water loops is employed to measure the upward heat transfer. The sideways and upward heat fluxes are measured by employing array of thermocouples at several different angular positions. Cable type heater with 3 mm in diameter and 4 m in length provides internal heating in the pool. Practically isothermal boundary conditions are provided at vessel boundaries with help of isothermal bath. A plate type heat

exchanger mounted in the isothermal bath circuit to increase cooling capacity of isothermal bath. The cooling circuit has two parallel paths, one for sidewall heat exchange and other for top heat exchange. Top heat exchanger flow is established by isothermal bath inbuilt recirculation pump. Second external recirculation pump was mounted in order to establish necessary flow rate for sidewall heat exchange. A digital flowmeter measures sidewall flow and an analog flowmeter measures top heat exchanger flow.

The diameter and height of the test section are respectively 62.0 cm and 53.0 cm as shown in Figure 7.2. The width of a slice is 9.0 cm. The front and back faces of the facility are insulated in order to decrease heat losses. Thickness of the vessel wall is 2.3 cm.

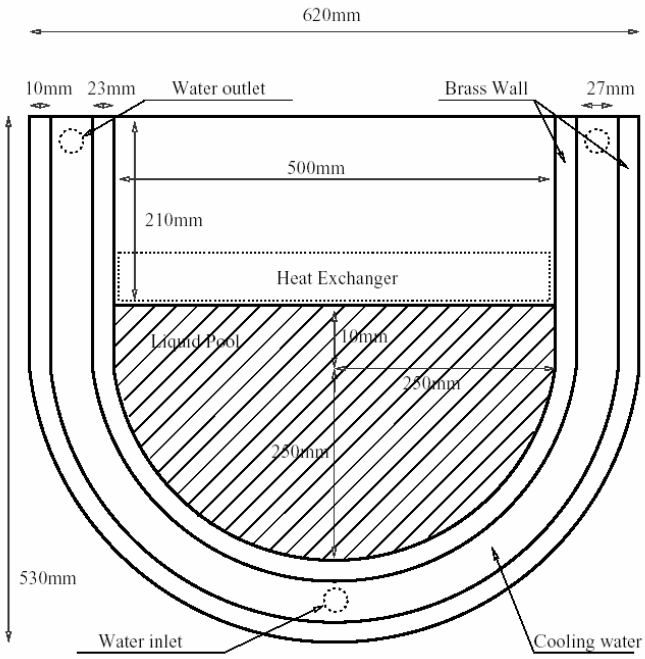

Figure 7.2: Schematic of the test section.

Total 64 K-type thermocouples are mounted to obtain data on sidewall heat flux, heat flux on top of pool, inlet and outlet water temperatures, as well as pool temperatures inside the vessel, and the upper heat exchanger. Location of thermocouples is shown in Figure 7.3.

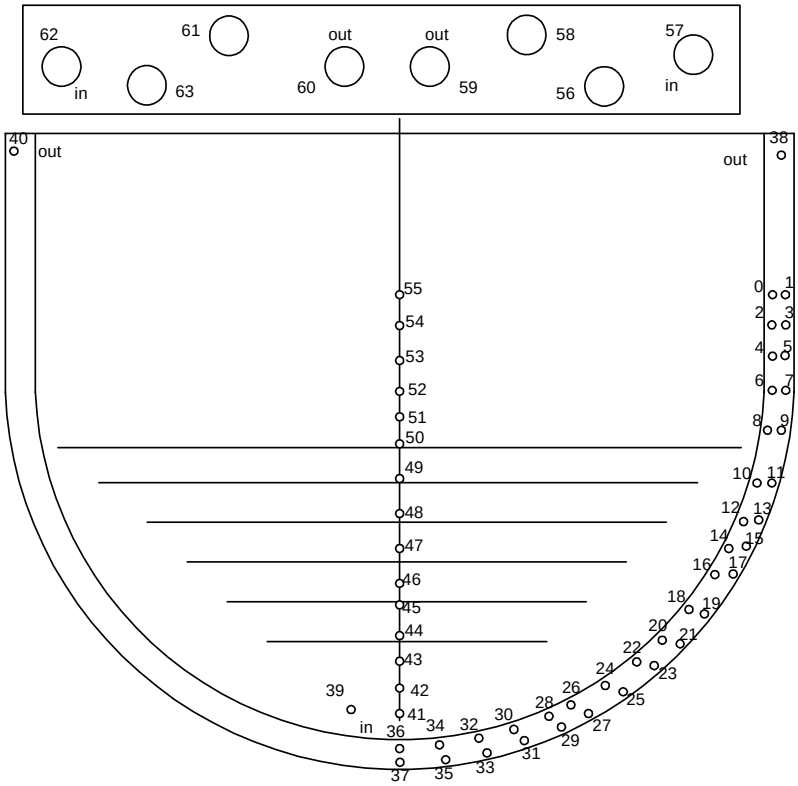

Figure 7.3: Thermocouple locations.

7.3 EXPERIMENTS

After completion of experimental set-up, we performed one two-layer experiment and three 3-layer experiments with different conditions. Short notes on each are given below.

7.3.1 Two-layer experiments

Paraffin oil (880 kg/m^3) and water (996.1 kg/m^3) were used as simulating liquids for this experiment. Power applied was equal to 1050 W. Flow rate through sidewall was ~ 7.5 l/min, and through upper heat exchanger ~ 4.4 l/min. Thickness of upper layer (paraffin oil) was 21 cm, and thickness of the lower layer (water) was 8 cm. In this experiment only upper layer was heated. Total duration of the experiment was equal to 3400 seconds.

7.3.2 Three-layer experiments

The experiments were done with three immiscible layers, v.i.z. chlorobenzene (996.1 kg/m^3), water (996.1 kg/m^3), and paraffin oil (880 kg/m^3). During all three experimental sessions chlorobenzene served as a lower layer with 8 cm depth, the water layer with depth of 21 cm was stratified on it, and above the water layer, a paraffin oil layer with depth 4 cm was added. The heat generation was set on only inside the water layer, so chlobenzene and paraffin oil were unheated. Flow rate through sidewall was ~ 7.5 l/min, and through upper heat exchanger ~ 4.4 l/min.
Raleigh number was the only factor, which changed for these three cases by changing the heating power.

- Experiment at Ra = 2.3621 e^{13}
- Experiment at Ra = 1.9133 e^{13}
- Experiment at Ra = 1.5117 e^{13}

The data obtained from both two and data analysis of the three-layer experiments is currently in progress.

8. MOLTEN POOL CONVECTION: FOREVER ANALYSIS

8.1 INTRODUCTION AND OBJECTIVES

The FOREVER (Failure Of REactor VEssel Retention) experimental program is concerned with the phenomena of melt pool convection and vessel failure occurring during the late phase of the in-vessel progression of a postulated severe accident in a Pressurised Water Reactor (PWR). Tests were performed at prototypic conditions of high temperature employing a $1:10^{th}$ scale reactor pressure vessel (RPV). Melt pool convection is established by heating a binary-oxide ($CaO\text{-}B_2O_3$) melt mixture with a special heater. In this case, the maximum melt pool temperature is maintained at $\sim 1100^0$C. The creeping of the vessel wall is obtained by pressurising the vessel up to 2.5 MPa, representing the depressurised severe accident scenario. The coupled melt pool convection and the multi-axial creep deformation process, under the thermal and the pressure loadings result expansion and elongation of the bottom of the lower head. The failure did not occur as the melt was cooled by, injecting water on top of melt. Experimental results along with the calculated important heat transfer parameters are presented on the interaction of melt with water supplied on its surface.

8.2 EXPERIMENTS

8.2.1 FOREVER experiments

A melt of an oxidic mixture: 30% CaO + 70% B_2O_3 (by weight) undergoes convection in the lower head due to the heat input by a specially designed heater. Heat input was maintained at a value such that, melt pool temperature attained a maximum value of $\sim 1000^0$C so that there will be a chance of crust formation near surface. The binary oxide melt has properties similar to those of $UO_2 + ZrO_2$. In this experiment, internal cooling is done by injecting water on the melt upper surface. Two big water tanks in series were used to condense the generated steam. There was no external cooling except for heat loss from outer surface of vessel by radiation and natural convection to air. Melt pool and vessel wall temperature were measured by thermocouples (TCs) and the vessel wall displacements were measured by linear displacement transducers. Temperatures and displacements were measured on the opposite sides of the vessel to determine the uniformity of the spatial distributions. One flow meter was used to measure the flow of steam at exit. Two pressure transducers were used to measure the pressure at exit of vessel and before flowmete, during the experiment. Two thermocouples were installed in the first condensing tank and one thermocouple was installed in the second condensing tank.

Values of the test parameters, *viz*, pressure to be applied and heat input to the melt pool were chosen for each test after a thorough pre-test analysis performed with the commercial ANSYS Multi-physics code (Previous report). The dimensions of steam flow path, condensing tank capacity and water injection rate were selected based on pre test analysis done using RELAP code. Pressure-temperature values had been maintained for such duration of time that there is a minimum of 5mm creep was observed before injecting water. Pressure relief test was done one day before the experiment, to see the relief time and modify loss coefficients in RELAP code.

Test vessel with its instrumentation and the induction furnace was kept inside the containment (Sehgal *et al.*, 2002a) for the sake of human safety. As in all the tests, the vessel was pre-heated to about 300^0C to avoid thermal shock. This also prevented thermal shock to the heating element. The containment temperature was kept below 50^0C by employing ventilation, in order to assure the proper operation of the instrumentation. It was necessary, because various instruments may not work properly at the higher temperature. Also special fans were employed to cool the displacement transducers as they received heat due to radiation from the vessel. It was important to maintain the temperature required for proper operation of the instrumentation.

Hot oxide melt, prepared in a SiC crucible in the induction furnace, is poured into the vessel through a funnel. Heater was kept at a lower power level so that the heater surface temperature is around poured melt temperature i.e. 1000 ^{o}C. After pouring the melt, the vessel opening was closed quickly and the vessel was made leak tight. Heater power is increased to deliver the desired power level and to maintain the oxide melt. Time was allowed to establish a steady state convection of melt inside the vessel. After the steady state temperature conditions were reached, pressure was applied to the vessel employing a balloon of argon gas. Heater power input and vessel pressure were kept constant till the time where sufficient creep in vessel was observed and then water was injected into vessel, where both gas pressurisation, heater power were stopped and the three valves leading out from vessel were opened. The following table gives the event sequence of transient after water pouring.

Table 1. Time of water injection into vessel.

Time (sec)	Event
0	Point of reference of data (dataset – 37685.0 s).
06	Heater off – All three valves were opened – water feed to vessel started. The water injected was about 5 Lit.
17	Water and melt contact
115	About 3 Lit of water is injected
385	About 2.8 Lit of water injected
495	About 3 Lit of water injected
945	About 2.5 Lit of water injected
1980	About 3 Lit of water injected
3520	About 5 Lit of water injected. The last injection.

8.2.2 Experimental results

The experimental data of condensing tank temperature, steam flow rate at exit, pressure near the flow meter and the pressure near pressure vessel are presented in Figure 8.1. For better understanding of the problem, the data selected is only for the initial 300 seconds, i.e. for the first two water injections, as it will be just an exponential cooling followed by this (the figure shows both filtered and nom filtered data). From Figure 8.1-b it was found that it took around 11 seconds from the time of valve opening to the time of water getting in contact with melt (which can be observed as the pressure peaks up). By the time water was in contact with the melt surface, the pressure in the vessel was about 7 bar, as the depressurization has been there for more than 11 seconds. As water came in contact with the melt surface, it was turbulent boiling with heated corium

particle ejection. The initial steam generation rate peaked up, and then came down drastically as the quantity of water added increased, thus cooling the upper surface of melt and forming a layer of crust. The upper surface was always maintained wet by supplying sufficient water so that there won't be complete evaporation from the melt surface.

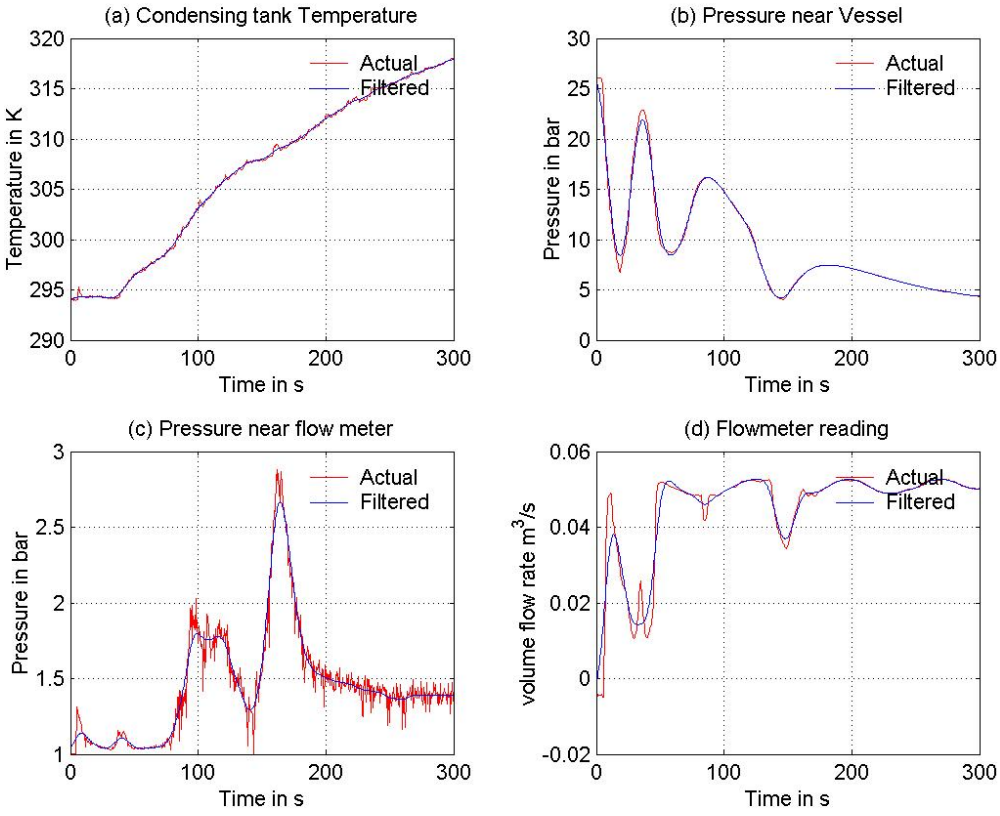

Figure 8.1: Experimental data (filtered and non filtered).

8.3 MODELLING

8.3.1 Modeling and nodalization

Forever experimental set up is modeled as shown in Figure 8.2. The vessel part of the problem is divided into two parts. One, that contains melt volume and water on top (Part B of Figure 8.2) and second one that contains rest of the set up (Part A of Figure 8.2). Calculations regarding the part B are done separately and the effect of this on the part A is considered in terms of the forced steam generation rate at a given state. The vessel is modeled as single volume and the three pipes are connected using vertical junctions to the vessel. The pipes have three on-off valves in-between to initiate the pressure relief (discharge) scenario. These three pipes are connected to one large diameter pipe with cross-junctions. This large diameter pipe in turn is connected in series connection of pipes of larger diameter and smaller diameter in order to have sufficient pressure drop near flow meter. The length of each pipe and expansion ratio required for proper pressure drop is estimated from pre-test analysis done using RELAP. The condensing tank at the exit is modeled as outlet boundary using time dependant volume.

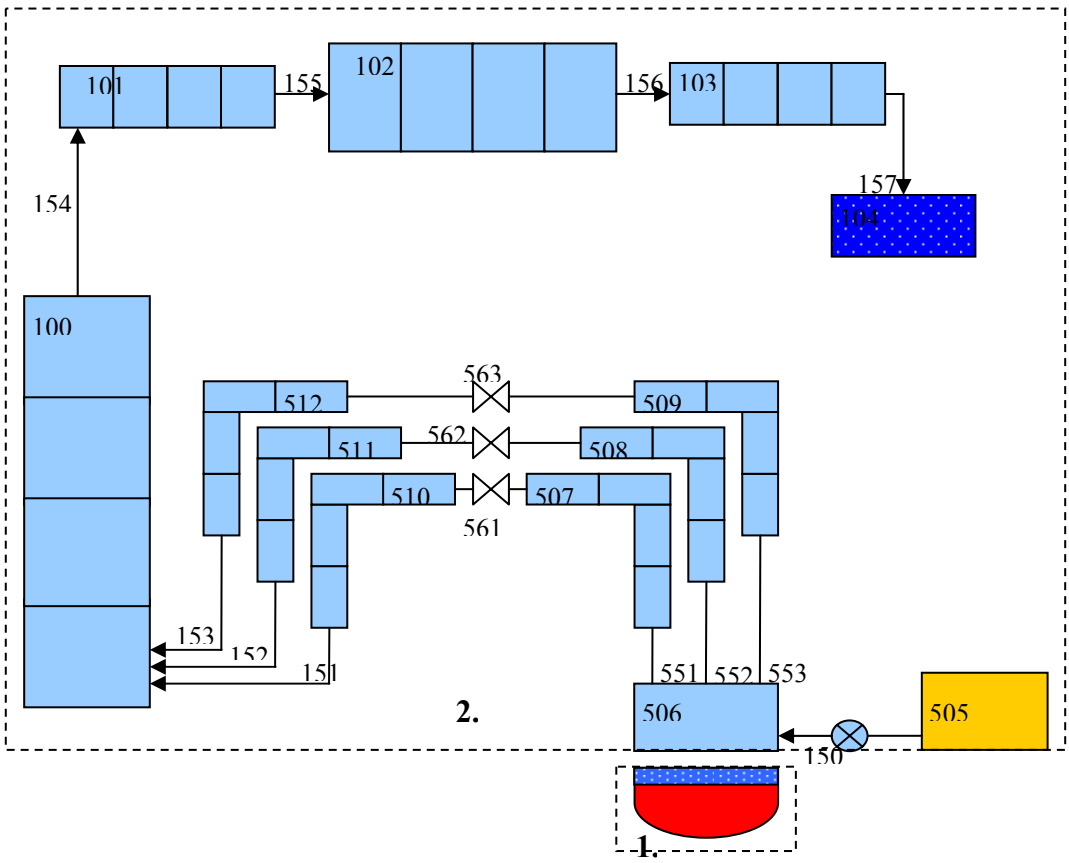

Figure 8.2: RELAP model for **FOREVER** experiment analysis.

8.3.2 Heat flux calculation

The cooling rate of corium is difficult to predict analytically because of large uncertainties in the morphology. What we have adopted is a simplified approach, where the energy required to raise the system pressure is combined to the energy going out of the system to find the net energy supplied to system (i.e. the net cooling rate). By using this approach, the result of steam generation rate inside the vessel, which was obtained from RELAP code, is shown in Figure 8.3-a. We can see the sudden spike in steam generation rate at the time when water came in contact with the melt surface. This maximum steam generation rate is around 0.11 kg/s, which decreases drastically to very low value, as more and more subcooled water is getting added. After some time this rate again peaks up as water injection is stopped and the water in vessel gets heated up and the heat from melt is used to generate the steam (latent heat). The second drop observed is due to the second addition of water and the process after this follows the same as mentioned above. Figure 8.3-b represents the latent heat removal rate in vessel, which corresponds to the steam generation rate at a given state. The maximum latent heat removal rate is around 1.8 MW/m^2. Figure 8.3-c and 8.3-d represent the cumulative mass and latent heat generated. The total energy liberated in initial 100 seconds is around 11.15 MJ (with latent heat of 8.0 MJ).

To cross check the above heat balance and to find initial maximum heat flux, consider second part of the problem i.e. part B as shown in Figure 8.3 (The melt part of the core). In this case as vessel expands, the height with respect to thermocouple locations change.

The initial height of the melt volume was 166 mm (corresponding to melt volume 11.5 m^3 and 0.5 m^3 more added for heater volume). Due to lateral expansion of 2 mm and vertical expansion of 14 mm, the melt level was dropped to 151 mm. Consider the temperature variation of centerline thermocouples for initial few seconds (Figure 8.4). The initial dropping rate of top 1 cm layer is 20 K/s, second 1 cm layer is 5 K/s and third 1 cm layer is 1.5K/s. Considering the 100 seconds data, the total energy liberated is 8151.1 kJ. This total energy is approximately equal to the RELAP calculation of liberated latent heat. If we consider the solid upper surface area of melt then with the initial 100 s data, the average heat flux obtained is 0.867 MW/m^2 (from part A we obtain average heat flux of 1.0 MW/m^2). For initial 100 seconds data, the average mass flux is around 0.38 kg/m^2s. If we consider each isothermal wave then, the quench front movement lies between the curve for isothermal 1000 ^oC and isothermal 950 ^oC as solidification temperature is 977 ^oC. For the first 1 cm depth, the solidification front moves at rate of 0.1 cm/s and next 1 cm depth it moves at 0.035cm/s. It will be slower and slower as depth increases.

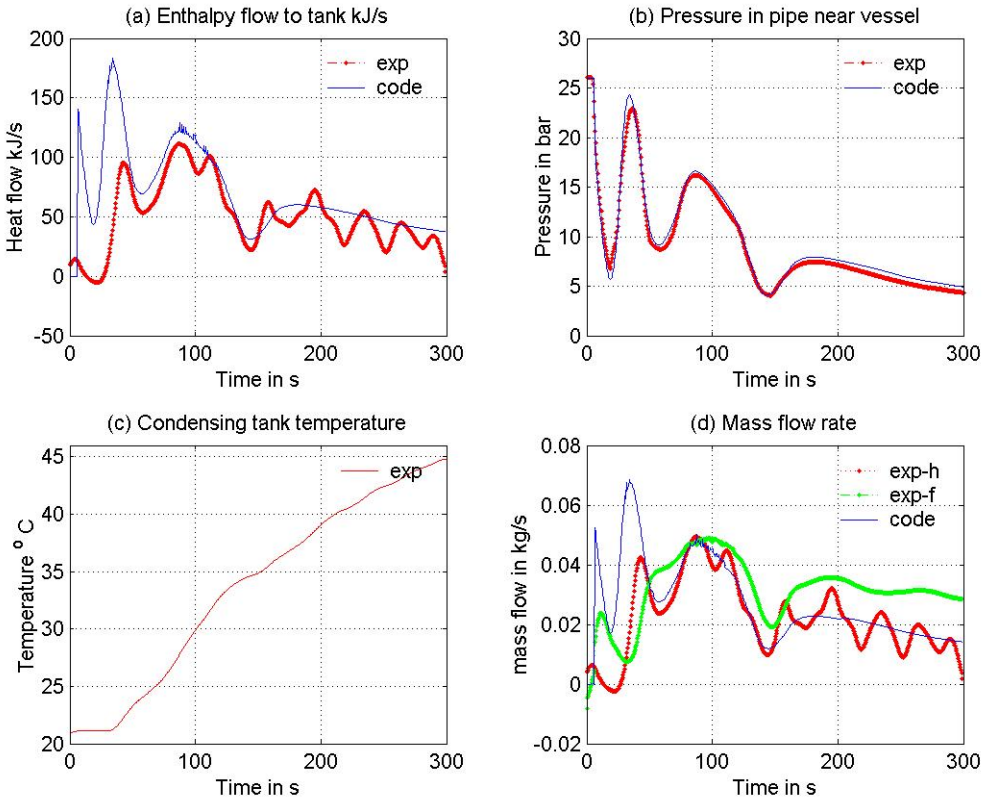

Figure 8.3: Experimental and code results comparison.

8.4 RESULTS

- In initial few seconds, the data seems to be quite scattered due to melt eruption on water contact. The picture of melt surface after test shows formation of large number of small volcanic structures and also the whole of mass is moved towards center showing bulge at the center. This increases heat transfer area is more than 50%.

- The predicted heat flux at 7 bar is about 2.0 MW/m^2. The heat flux calculated from the experimental data obtained and considering solid surface area of melt, was 2.0 MW/m^2. If we consider real surface area (which will be higher than the area considered) then the heat flux calculated seems to be a over prediction, and actual heat flux may be lower than 2.0 MW/m^2

- The energy liberated in initial 100 seconds calculated from melt pool temperature is 9.55 MJ and calculated from water evaporation rate is 11.15 MJ. This imbalance in heat can be justified with the heat content of the vessel and structures (including heater).

- Initial average mass flux obtained was 0.38kg/m^2 and average heat flux was 0.88 MW/m^2. These values are comparable to the values obtained in RASPLAV-2 experiment, which are 0.46kg/ m^2 and 1.0 MW/m^2.

- For the first 1 cm depth, the solidification front moves at rate of 0.1 cm/s and next 1 cm depth it moves at 0.035cm/s. The crack propagation or water ingression will be still slower and will be limited to certain depth of corium. In our experiment, the top crust formation was about 5 to 7 cm.

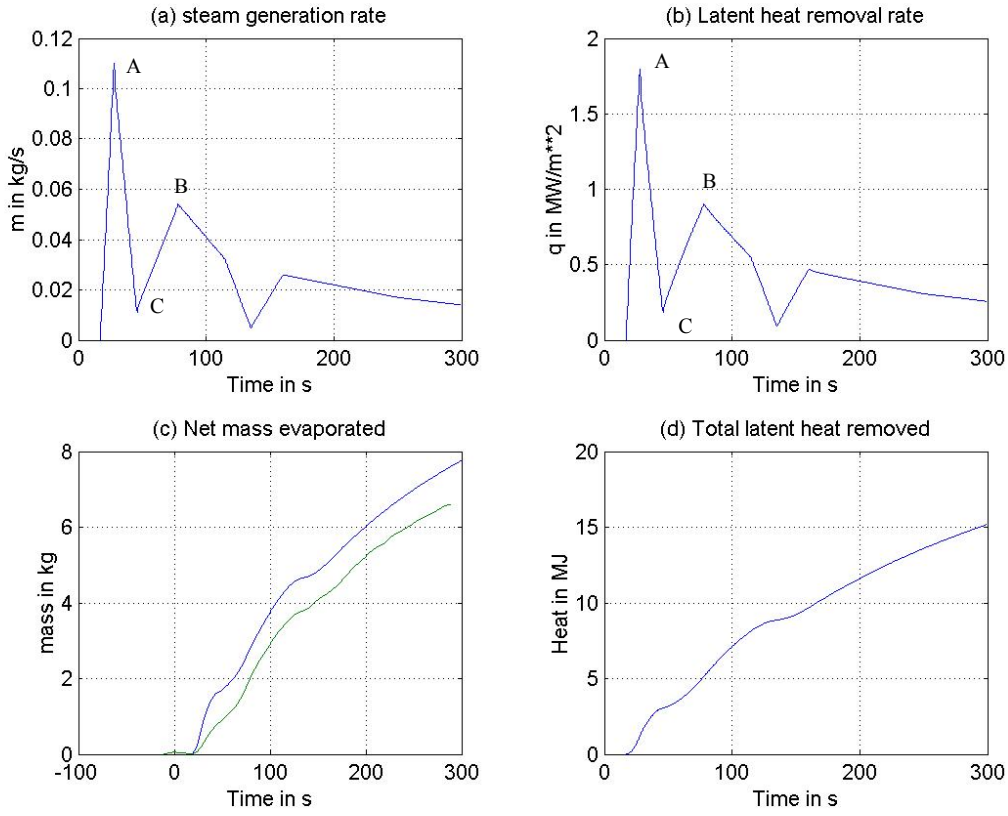

Figure 8.4: Heat flux and mass generation rates.

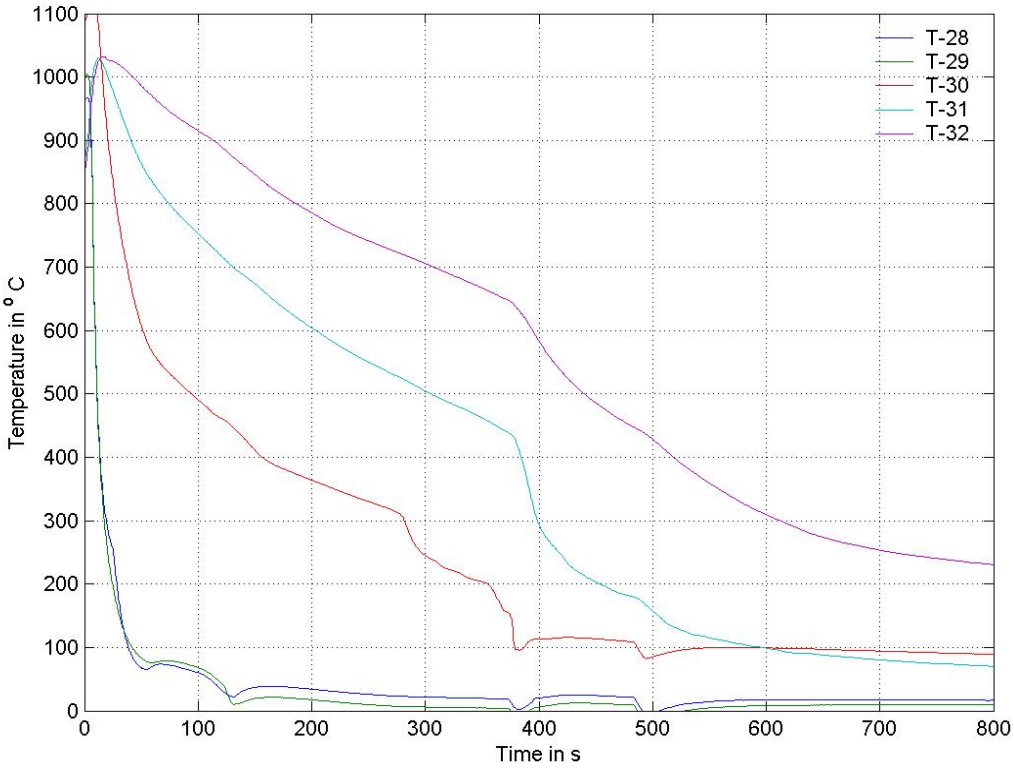

Figure 8.5: Melt centerline temperature variation for initial 800 seconds.

9. LIST OF PUBLICATIONS

The research program has resulted in many peer-reviewed publications in the year 2002. We are presenting here a selection which provides, (1) the description of the experimental program and results on melt droplet-water interaction, melt pool coolability, vessel creep and rupture; and (2) the description of the analysis models and results dealing with the thermal hydraulic behavior occurring during the melt-water interaction, melt pool coolability, and melt-vessel interaction processes.

1. Park, H. S., Hansson R. C., and Sehgal, B. R., "Impulsive Shock Induced Single Drop Steam Explosion Visualized by High-Speed X-ray Radiography and Photography Metallic Melt," The 10th International Topical Meeting on Nuclear Reactor Thermal Hydraulics (NURETH10), Seoul, Korea, Oct. 5~9, (2003).

2. Giri,A., Park, H. S., Hansson R. C., and Sehgal, B. R., "Bubble Dynamics and Stability Analysis in Liquid-Vapor-Liquid System," The 10th International Topical Meeting on Nuclear Reactor Thermal Hydraulics (NURETH10), Seoul, Korea, Oct. 5~9, (2003).

3. Park, H. S., Hansson, R. C., and Sehgal, B. R., "Fine Fragmentation Process observed by X-ray Radiography," The European-Japanese Two-Phase Flow Group Meeting, Siena, Italy, September 21~27, (2003).

4. Giri, A., Park, H. S., and Sehgal, B. R., "Analysis of Bubble Dynamics in Explosive Boiling of Droplet with Fine Fragmentation," The European-Japanese Two-Phase Flow Group Meeting, Siena, Italy, September 21~27, (2003).

5. Park, H. S., Hansson R. C., and Sehgal, B. R., "Visualization of Dynamic Fragmentation of Molten Liquid Droplet in Liquid Coolant," The 2nd International Conference on Heat Transfer, Fluid Mechanics and Thermodynamics (HEFAT-2003), Paper No. SB2, Victoria Falls, Zambia, 23-26 June, (2003).

6. Park, H. S., Hansson R. C., and Sehgal, B. R., "Continuous High-Speed X-ray Radiography to Visualize Dynamic Fragmentation of Molten Liquid Droplet in Liquid Coolant," CD-Rom Proceeding of the 4th Pacific Symposium on Flow Visualization and Image Processing (PFSVIP4), PSFVIP4-4090, Chamonix, France, June 3~5, (2003).

7. Park, H. S., Hansson, R. C., and Sehgal, B. R., "Micro-interactions observed during Explosive Boiling in Liquid-Vapor-Liquid System," The 41th European Two-Phase Flow Group Meeting, Hurtigruten, Norway, May 12~14,(2003).

8. Giri, A., Park, H. S., Hansson R. C., and Sehgal, B. R., "Bubble Dynamics and Stability Analysis in Liquid-Vapor-Liquid System," The 41th Europian Two-Phase Flow Group Meeting, Hurtigruten, Norway, May 12~14,(2003).

9. Park, H. S., Hansson R. C., and Sehgal, B. R., "Single Drop Melt Fragmentation Observed by High-Speed X-ray Radiography and Photography," CD-Rom Proceeding of the 11th International Conference on Nuclear Engineering (ICONE11), ICONE11-36327, Keio Plaza Inter-Continental Shinjuku, Tokyo, Japan, April 20~23, (2003).

10. Konovalikhin, M.J., Jasiulevicius, A., Sehgal, B.R., "Debris bed coolability in the BWR pressure vessel", Proceedings of 6th ASME-JSME Thermal Engineering Joint Conference, Kohala Coast, Havaii, USA, March 16-20, 2003.

11. Sehgal, B.R., Konovalikhin, M.J., Jasiulevicius, A., "Debris bed coolability in the BWR pressure vessel", Proceedings of HEFAT2003, 2nd Conference on Heat Transfer, Fluid Mechanics and Thermodynamics, Victoria Falls, Zambia, June 23-26, 2003.

12. Sehgal, B.R., Giri, A., Karbojian, A., Theertan, A., "Experiment on the lower head vessel failure under coupled melt pool convection and creep", Proceedings of HEFAT2003, 2nd Conference on Heat Transfer, Fluid Mechanics and Thermodynamics, Victoria Falls, Zambia, June 23-26, 2003.

13. Sehgal, B.R., Giri, A., Karbojian, A., Theertan, A., "Effect of penetration on the lower head vessel failure under coupled melt pool convection and creep", Proceedings of SMIRT 17 Conference, Czech Republic, August 2003.

14. Jasiulevicius, A., Sehgal, B.R., "COMECO experiments on molten pool coolability enhancement in the BWR lower head with CRGTs". Proceedings of NURETH-10 conference, Seoul, Korea, October 5-9, 2003.

15. Sehgal, B. R., "Stabilization and termination of severe accidents in LWRs" The 10th International Topical Meeting on Nuclear Reactor Thermal Hydraulics (NURETH10), Seoul, Korea, Oct. 5-9, (2003).

10.CONCLUDING REMARKS

We believe that significant technical advances have been achieved during the course of these studies at RIT/NPS during 2003. It was found that:

(1) MISTEE Program:

- A series of experiments on single drop steam explosions was performed to investigate the fine fragmentation process of a metallic melt drop in various thermal conditions. For the first time, transient fine fragmentation process of a melt drop during steam explosion was quantified.

- Visual observation with high-speed photography and X-ray radiographs indicated that the small-scale stratified explosion initiated at the side edge of a droplet propagated along the melt surface for highly subcooled water. The fragment jets were ejected from the wavy boundary of the interaction zone. These jets can be an evidence of a micro-jet formation also observed in the cavitation process.

- The secondary explosions of larger melt fragments separated from the wavy surface of the interaction zone. This secondary explosion was not observed in tests with water temperature less than 40^{o}C.

- A shell of fragmented melt particle near the vapor bubble boundary was observed during the explosions. The maximum expansion diameter of fragmented particles and vapor bubble reached 3~3.5 times the initial diameters.

- Single drop vapor explosions in all tests initiated by an impulsive shock wave resulted in the complete collapse of a steam-air pocket in the case of above 40 ^{o}C water tests. This collapse has two counter effects; suppression of vapor explosion by supplying non-condensable air and extra triggering source.

- A separate quenching experiment that employed a hot stainless steel ball was performed to investigate the thermal behavior of the molten droplet prior to the triggering process of the steam explosion. The experiments will provide a data set to verify the theoretical model for the film boiling process in the stage of development.

- The analyses on the vapor bubble dynamics and stability provided an insight of the molten droplet fragmentation and associated energy (pressure) generation. It was shown that approximately 70% of a molten droplet was finely fragmented after the second collapse of vapor bubble induced by the steam explosions.

(2) POMECO Program

- The POMECO experiments had shown that the presence of the control rod guide tubes offers a significant additional cooling capacity for the particulate debris bed, which leads to enhancement of the dryout heat flux and the quenching rate. Heat removal rate through CRGT structure was found to be 10-15 kW depending on the surrounding porous media and temperature regime. Water flow rates in the CRGT

result in additional enhancement of the dryout heat flux and intensification of quenching process.

- The Lipinski model with addition of CRGT coolability potential was employed to analyze the POMECO dryout experiments. Reasonable agreement between the experimental and calculated results was obtained.

- Characteristic times for quenching were computed by the model, which combines parameters of the process (V, p_{over}, T_{sol}, T_w, W), geometry (A_{bed}, d_{dwnc}) and physical properties (H_{fg}, $C_{p,w}$, ρ_w, μ_w, $C_{p,sol}$, ρ_{sol}, ε). Good agreement between experimental and calculated results has been achieved for the POMECO experiments and the high temperature debris bed experiment at the COMECO facility.

(3) COMECO Program

- A series of experiments at the COMECO facility with the presence of a downcommer in the melt pool are being performed. The preliminary experimental findings indicate, that the presence of the downcommer reduces the melt pool layer quenching times. However, the effect of the downcommer is not as great as expected and as indicated by the previous series of POMECO experiments for the particulate debris bed coolability. The experimental program will continue and the obtained results will be presented and analyzed.

- The analysis of previous set of COMECO experiments (with a control rod guide tube model in the test section) was carried out. The melt pool quenching times, crust growth and water ingression rates were analyzed.

- The analysis of the experimental results was carried out for various phases of the quenching process. The zero-dimensional model derived from the heat balance of the test section provides a good prediction for the quenching times, recorded during the COMECO experiments. It shows that the efficiency of the heat removal capacity offered by the CRGT's increases with the crust thickness. The bulk cooling resulted in high heat fluxes during the first moments of the experiments. The Farmer's model for the crust growth and water ingression provided good estimations of the measured processes.

- The COMECO experimental program will continue and the experimental database for the melt pool coolability with the presence of a downcommer will be compiled. Also, the analytical work in the melt coolability – related areas will be pursued.

(4) SIMECO Program

- The SIMECO experiments were restarted to investigate the melt pool convection in multi-layer configuration which has metallic melt layers on the top and bottom and oxidic melt layer in the middle of the melt pool. The experimental results were compared to those from the previous SIMECO experiments with the uniform and two/layer melt pool configuration

(5) FOREVER Analysis

- In initial few seconds, the data seems to be quite scattered due to melt eruption on water contact. The picture of melt surface after test shows formation of large number of small volcanic structures and also the whole of mass is moved towards center showing bulge at the center. This increases heat transfer area is more than 50%.

- The predicted heat flux at 7 bars is about 2.0 MW/m^2. The heat flux calculated from the experimental data obtained and considering solid surface area of melt, was 2.0 MW/m^2. If we consider real surface area (which will be higher than the area considered) then the heat flux calculated seems to be a over prediction, and actual heat flux may be lower than 2.0 MW/m^2

- The energy liberated in initial 100 seconds calculated from melt pool temperature is 9.55 MJ and calculated from water evaporation rate is 11.15 MJ. This imbalance in heat can be justified with the heat content of the vessel and structures (including heater).

- Initial average mass flux obtained was 0.38kg/m^2 and average heat flux was 0.88 MW/m^2. These values are comparable to the values obtained in MACE experiment, which are 0.46kg/ m^2 and 1.0 MW/m^2.

- For the first 1 cm depth, the solidification front moves at rate of 0.1 cm/s and next 1 cm depth it moves at 0.035cm/s. The crack propagation or water ingression will be still slower and will be limited to certain depth of corium. In our experiment, the top crust formation was about 5 to 7 cm.

ACKNOWLEDGEMENTS

These studies will be continued in the current research program at RIT/NPS sponsored by the Swedish Nuclear Power Inspectorate (SKI), the Swiss Federal Nuclear Inspectorate (HSK). the European Union, and Swedish and Finnish power companies also supported these research efforts.

www.ski.se

STATENS KÄRNKRAFTINSPEKTION
Swedish Nuclear Power Inspectorate

POST/POSTAL ADDRESS SE-106 58 Stockholm
BESÖK/OFFICE Klarabergsviadukten 90
TELEFON/TELEPHONE +46 (0)8 698 84 00
TELEFAX +46 (0)8 661 90 86
E-POST/E-MAIL ski@ski.se
WEBBPLATS/WEB SITE www.ski.se